



HAL
open science

Non-specific interactions govern cytosolic diffusion of nanosized objects in mammalian cells

Fred Etoc, Elie Balloul, Chiara Vicario, Davide Normanno, Domenik Lisse,
Assa Sittner, Jacob Piehler, Maxime Dahan, Mathieu Coppey

► To cite this version:

Fred Etoc, Elie Balloul, Chiara Vicario, Davide Normanno, Domenik Lisse, et al.. Non-specific interactions govern cytosolic diffusion of nanosized objects in mammalian cells. *Nature Materials*, 2018, 17 (8), pp.740-746. 10.1038/s41563-018-0120-7 . hal-01871099

HAL Id: hal-01871099

<https://hal.sorbonne-universite.fr/hal-01871099>

Submitted on 10 Sep 2018

HAL is a multi-disciplinary open access archive for the deposit and dissemination of scientific research documents, whether they are published or not. The documents may come from teaching and research institutions in France or abroad, or from public or private research centers.

L'archive ouverte pluridisciplinaire **HAL**, est destinée au dépôt et à la diffusion de documents scientifiques de niveau recherche, publiés ou non, émanant des établissements d'enseignement et de recherche français ou étrangers, des laboratoires publics ou privés.

1 **Non-specific interactions govern cytosolic diffusion of nano-sized** 2 **objects in mammalian cells**

3
4 Fred Etoc^{1,§}, Elie Balloul^{1,†}, Chiara Vicario^{1,†,§}, Davide Normanno^{1,2,*}, Domenik Liße³, Assa
5 Sittner⁴, Jacob Piehler³, Maxime Dahan^{1,*}, Mathieu Coppey^{1,*}

6
7 1, Laboratoire Physico-Chimie, Institut Curie, CNRS UMR168, PSL Research University,
8 Université Pierre et Marie Curie-Paris 6. 11 rue Pierre et Marie Curie, 75248 Paris - Cedex
9 05, France

10
11 2, Centre de Recherche en Cancérologie de Marseille, CNRS UMR7258, Inserm U1068, Aix-
12 Marseille Université UM105, Institut Paoli-Calmettes. 27 boulevard Leï Roure, 13273
13 Marseilles - Cedex 09, France

14
15 3, Division of Biophysics, Department of Biology, Osnabrück University. BarbarasträÙe 11,
16 49076 Osnabrück, Germany

17
18 4, Department of Infectious Diseases, Israel Institute for Biological Research. POB 19,
19 7410001 Ness Ziona, Israel

20
21 † Equally contributed to this work

22
23 § Current address: Center for Studies in Physics and Biology, The Rockefeller University.
24 1230 York Avenue, New York, NY 10065, USA (F.E.). Centre for Genomic Regulation, The
25 Barcelona Institute of Science and Technology. Carrer del Dr. Aiguader 88, 08003 Barcelona,
26 Spain (C.V.)

27
28 * Corresponding authors: davide.normanno@inserm.fr, maxime.dahan@curie.fr,
29 mathieu.coppey@curie.fr

30 31 32 **Abstract**

33
34 The diffusivity of macromolecules in the cytoplasm of eukaryotic cells varies over orders of
35 magnitude and dictates the kinetics of cellular processes. However, a general description
36 associating the Brownian or anomalous nature of intracellular diffusion to the architectural
37 and biochemical properties of the cytoplasm has not been achieved. Here, we measure the
38 mobility of individual fluorescent nanoparticles in living mammalian cells to obtain a
39 comprehensive analysis of cytoplasmic diffusion. We identify a correlation between tracer
40 size, its biochemical nature, and its mobility. Inert particles with size equal or below 50 nm
41 behave as Brownian particles diffusing in a medium of low viscosity with negligible effects of
42 molecular crowding. Increasing the strength of non-specific interactions of the nanoparticles
43 within the cytoplasm gradually reduces their mobility and leads to sub-diffusive behaviour.
44 These experimental observations and the transition from Brownian to sub-diffusive motion
45 can be recapitulated in a minimal phenomenological model.

46
47
48
49

50 Cytoplasmic diffusion plays a fundamental role in many cellular processes. For instance,
51 signalling pathways are activated by chemical species that diffuse and react in the
52 microenvironment of the cytoplasm, therefore molecular diffusion dictates the dynamics of
53 cellular responses¹, such as MAPK activation² or the kinetics of search processes³. Assessing
54 the physical nature of the cytoplasm, and its consequences on the mobility of biomolecules, is
55 essential for understanding, and eventually controlling, biochemical processes in living cells.

56
57 The cytoplasm of eukaryotic cells is generally described as a bi-phasic poro-elastic
58 medium^{4,5}, composed of a fluid phase, the cytosol, consisting of water and soluble proteins,
59 and a solid phase consisting of the cytoskeleton, endomembranes, organelles, and
60 supramolecular complexes⁶. Starting from the seminal work on the mobility of IgG and BSA⁷,
61 a plethora of –often conflicting– findings about cytosolic diffusion has been reported in the
62 literature (for recent reviews see Ref. 8,9). Early fluorescence recovery after photo-bleaching
63 (FRAP) experiments with inert Dextran and Ficoll pointed to a cytosol slightly (1 to 4 times)
64 more viscous than water^{10,11}, while experiments with various proteins, as reviewed in Ref. 6,
65 yielded to an apparent cytosol viscosity varying between 0.007 (for Insulin¹²) and 0.49 (for
66 GFP¹³). Theoretical work¹⁴ as well as *in vitro* experiments in dense, crowded solutions and in
67 cell extracts^{15,16} have also suggested that diffusion in the cytoplasm could deviate from
68 Brownian motion. Experiments in cells have led to the observation of both phenomena:
69 Brownian diffusion^{17,18} and sub-diffusive motion¹⁹⁻²¹. Since all these results have been
70 obtained with a variety of tracers and in different experimental conditions, a fundamental,
71 long-lasting²² and yet unresolved question is whether a unified framework can account for the
72 large variability of behaviours observed for cytosolic diffusion.

73
74 Two major classes of phenomena can affect the mobility of a tracer and potentially lead to
75 sub-diffusion. First, obstacles are expected to induce steric hindrance, limiting the accessible
76 space, and thereby slow down diffusion^{15,23}. We refer to these geometric effects as
77 “obstructive molecular crowding” caused by a high concentration of macromolecules in the
78 cytoplasm^{18,24}. Second, biochemical (e.g. electrostatic or hydrophobic) interactions with
79 elements of the cytoplasm, referred here as “non-specific interactions”, can give rise to
80 transient immobilization and reduced mobility. In the present work, using single-particle-
81 tracking²⁵ of fluorescent nanoparticle (NP) tracers, we show that inert objects, with size below
82 ~75 nm, are not affected by obstructive molecular crowding and behave as Brownian particles
83 diffusing in a medium of low viscosity. For tracers with given size (~25 nm) but with
84 increasing levels of non-specific interactions, we find that the effective diffusivity is
85 progressively slowed down by more than 3 orders of magnitude while diffusion gradually
86 becomes anomalous. We show that a simple continuous time random walk model, in which
87 the strength of non-specific interactions is captured into a single parameter, is sufficient to
88 recapitulate the intracellular mobility of all the different probes analysed.

90 **Tracers of similar size have different diffusivities**

91
92 To systematically inspect the cytoplasmic mobility of nano-sized objects, we first established
93 a methodology to quantify and compare the diffusivity of two different NPs with similar size:
94 rhodamine-doped, streptavidin-coated polystyrene/polymethacrylate particles (called “25nm
95 Rho-NPs”, but of measured diameter $35\text{nm} \pm 8\text{nm}$) and Amino (PEG) 655 ITK™ Quantum
96 Dots (called “QDs”, about 20nm in diameter²⁶). Probes were internalized in HeLa cells
97 through pinocytotic loading²⁷, which allows the delivery of 20 to 50 individual NPs per cell.
98 Control experiments ensured that pinocytotic loading effectively yielded dispersed NPs in the

99 cytosol of viable, living cells (see Methods, Supplementary Fig. 1-7, and Supplementary
100 Video 1-5).

101

102 Cytoplasmic diffusion of individual NPs was recorded by time-lapse microscopy and
103 quantified using single-particle-tracking analysis. From each individual trajectory, we
104 extracted two complementary parameters. First, we estimated the mobility at short time scales
105 computing the time-averaged Mean Square Displacement (taMSD) at 60 ms, $\langle r_{60\text{ms}}^2 \rangle_T$ (see
106 Methods). For convenience, we express this observable in terms of a diffusion coefficient
107 $D_{60\text{ms}} = \langle r_{60\text{ms}}^2 \rangle_T / 4\delta$, (with $\delta = 60\text{ms}$). Second, we characterized the mobility at long time
108 scales computing the anomalous exponent. We selected trajectories longer than 40 time points
109 and fitted each individual taMSD curve with a general model of diffusion $\langle r^2 \rangle_T \sim t^\alpha$, from
110 which we determined the anomalous exponent α as a single fitting parameter. To represent
111 the behaviour of the whole population of NPs in each condition, the distribution of the
112 parameters α and $D_{60\text{ms}}$ arising from each individual trajectory was represented as a two-
113 dimensional density map²⁸ (Fig 1). Given the robustness with respect to the choice of
114 parameters used for their computation (Supplementary Fig. 8), α - $D_{60\text{ms}}$ maps can be used as
115 benchmark to systemically compare the mobility of nano-sized objects in the cytoplasm of
116 living cells.

117

118 In the case of 25nm Rho-NPs (Fig. 1a,b), we found a predominant sub-population with $D_{60\text{ms}}$
119 peaking at $1.34 \pm 0.07 \mu\text{m}^2 \cdot \text{s}^{-1}$ (all values are mean \pm standard error of the mean (SEM), the
120 number N of trajectories considered in the analysis is reported in figure captions) and
121 $\alpha = 0.92 \pm 0.01$, close to 0.96 ± 0.02 , the value obtained for simulated Brownian particles
122 (see Methods). In addition to (fast) Brownian particles, 25nm Rho-NPs presented a second
123 (slow) population ($\sim 30\%$) with reduced instantaneous mobility, $D_{60\text{ms}} = 0.51 \pm$
124 $0.05 \mu\text{m}^2 \cdot \text{s}^{-1}$, and strongly sub-diffusive $\alpha = 0.18 \pm 0.02$ (see Supplementary Fig. 9 and
125 Methods).

126

127 For QDs, we found a single, broad peak in the α - $D_{60\text{ms}}$ plane (Fig. 1c,d). The distribution of
128 $D_{60\text{ms}}$ spanned more than three orders of magnitude, as for 25nm Rho-NPs, but peaked at
129 $0.15 \pm 0.01 \mu\text{m}^2 \cdot \text{s}^{-1}$, one order of magnitude smaller than for 25nm Rho-NPs. Furthermore,
130 the exponent $\alpha = 0.71 \pm 0.01$ pointed to a deviation from Brownian diffusion. As reference,
131 the distribution obtained with the same QDs in a glycerol solution (80% v/v) is more
132 homogeneous (Fig. 1e), with $\alpha \sim 1$, indicative of Brownian diffusion (Fig. 1f). Thus, the
133 heterogeneity in QDs mobility, its deviation from Brownian diffusion and from the behaviour
134 of 25nm Rho-NPs does not arise from a broad size distribution of QDs nor from specific
135 features of single-particle-tracking analysis but is intrinsic to the intracellular mobility of
136 QDs.

137

138 **Rho-NPs undergo Brownian motion for sizes up to 50nm**

139

140 We next investigated the range of particle sizes over which the observation of Brownian
141 motion was valid by comparing the mobility of Rho-NPs of increasing dimension (15, 25, 50
142 and 75 nm in diameter, see Supplementary Fig. 10). 75nm Rho-NPs were microinjected since
143 pinocytic loading does not work for large objects. In the α - $D_{60\text{ms}}$ plane, NPs below or equal to
144 50 nm had similar features, majorly peaking at $\alpha \sim 1$ and with $D_{60\text{ms}}$ on the order of $1 \mu\text{m}^2 \cdot \text{s}^{-1}$
145 (Fig. 2a-c). Remarkably, $D_{60\text{ms}}$ decreased as the inverse of NPs size, as expected for diffusion
146 in a homogeneous medium, and the apparent cytoplasmic viscosity –estimated using the
147 Stokes-Einstein equation– was 10-15 times higher than that of water (Supplementary Table

148 1), i.e. about five times higher than previous reports for the viscosity of the fluid phase of the
149 cytoplasm^{29,30}.

150

151 The diffusive properties of 75nm Rho-NPs were strikingly different (Fig. 2d). The average
152 $D_{60\text{ms}}$ was $0.22 \pm 0.03 \mu\text{m}^2 \cdot \text{s}^{-1}$ (with a median value of $0.015 \mu\text{m}^2 \cdot \text{s}^{-1}$), much smaller than
153 the three other samples. Furthermore, trajectories were strongly sub-diffusive, with low α
154 values (0.56 ± 0.03). We concluded that there is a clear cut-off, between 50 and 75 nm, in the
155 size dependence of NPs mobility.

156

157 **QDs show sub-diffusive behaviour**

158

159 To assess the departure of QDs from Brownian diffusion, we computed the ensemble average
160 of all individual taMSDs, $\langle\langle r^2 \rangle_T \rangle_E$. Although $\langle\langle r^2 \rangle_T \rangle_E$ grew sub-linearly (Fig. 3a and
161 Supplementary Fig. 11), a single exponent α failed to describe the experimental data since it
162 evolved from 1 at short time scales (tens of milliseconds) down to 0.7 at time scales on the
163 order of seconds. We found that this variation of α was due to the ensemble averaging
164 procedure, which samples trajectories unevenly. Diffusing NPs can escape the volume of
165 observation, determined by the depth of field of the microscope ($\sim 500\text{nm}$), resulting in an
166 exponential distribution of trajectory lengths (mean duration of 1.4s, Supplementary Fig. 12).
167 Due to the limited imaging depth, particles with small $D_{60\text{ms}}$ tend to stay longer within the
168 observation volume and, thus, yield longer trajectories than fast diffusing particles³¹.
169 Therefore, averaging together all individual taMSDs led to a progressive decrease with time
170 of the slope of the ensemble average of taMSDs, as the contribution of slow NPs becomes
171 predominant at longer times (Supplementary Fig. 13).

172

173 To overcome this bias, we considered trajectory datasets homogeneous in length. Specifically,
174 we chose trajectories lasting at least N steps to build the ensemble average of taMSDs,
175 $\langle\langle r^2 \rangle_{T \geq N\Delta t} \rangle_E$, which we computed up to time $N \cdot \Delta t$. By doing so, we ensured that all
176 trajectories contributed equally to the ensemble average over the whole time span considered.
177 In Fig. 3b, $\langle\langle r^2 \rangle_{T \geq N\Delta t} \rangle_E$ is plotted in log-log scale for N equal to 30, 75 and 150 steps
178 (corresponding, respectively, to a time window of 0.9, 2.25, and 4.5s). Strikingly, even if the
179 three MSD curves include varying partitioning of the different QDs behaviours (the longer the
180 trajectories are, the slower the mobility is), all curves are linear in log-log scale with an
181 identical exponent $\alpha \sim 0.82$, indicative of a uniform behaviour. We thus concluded that QDs
182 diffusion can be well described by a homogeneous sub-diffusive process.

183

184 **QDs sub-diffusion arises from non-specific interactions**

185

186 We first inspected if confinement by the cytoskeleton or internal membranes could explain
187 the observed QDs sub-diffusion. We used different drugs known to disrupt the actin
188 meshwork, the microtubule network, and the Golgi apparatus (Latrunculin-A, Nocodazole,
189 and Brefeldin-A, respectively), but we found no substantial change in the sub-diffusive
190 behaviour of QDs (Supplementary Fig. 14). We also analysed QD trajectories using a
191 confined diffusion model to fit individual $\langle r^2 \rangle_T$ curves. We found no strong evidence for
192 confinement with and without drugs (Supplementary Fig. 15 and Supplementary Table 2). We
193 concluded that, for NPs below the critical cut-off size of 75 nm, geometric restrictions due to
194 confinement within the cytoskeleton meshwork or the Golgi have no pronounced effects on
195 cytoplasmic mobility.

196

197 We next aimed at discriminating between steric hindrance due to high density of obstacles
198 and transient non-specific interactions. In the latter case, anomalous diffusion would arise
199 from a broad distribution of interaction times, whose specific signature would be the loss of
200 equivalence between temporal and ensemble averages, a phenomenon called ergodicity
201 breaking³². We therefore performed a simple statistical test for ergodicity³³. Following the
202 approach proposed by Weigel *et al.*³⁴, we compared the distribution of time-averaged square
203 displacements (shown in Fig. 1c) to the distribution of ensemble-averaged square
204 displacements. As visible in Fig. 3c, the distribution of time-averaged square displacements is
205 much broader than the distribution of ensemble-averaged square displacements, an indication
206 of ergodicity breaking (observed also under Brefeldin-A and Latrunculin-A treatments, see
207 Supplementary Fig. 16a). In contrast, QDs diffusing in glycerol satisfied ergodicity (Fig. 3d).
208 We also observed aging in the trajectories^{34,35} (Supplementary Fig. 16b), an additional
209 signature of ergodicity breaking. Altogether, our analysis strongly supports the view that non-
210 specific interactions rather than obstructive molecular crowding are at the origin of sub-
211 diffusion.

212

213 To further demonstrate the role of non-specific interactions, we hypothesized that diffusion
214 should be affected by the surface properties of the tracer and we thus screened QDs with
215 different surface chemistries and charges. We found the distribution of $D_{60\text{ms}}$ to strongly
216 depend on the surface coating of QDs (Fig. 3e) but with no correlation between the
217 electrostatic potential and the degree of reduced mobility (Supplementary Table 3). Although
218 the passivation of QDs surface greatly increased mobility, neither PEG nor streptavidin
219 coating resulted in QDs as diffusive as Rho-NPs. Most likely, the strongly interacting QDs
220 core still contributed to non-specific binding even after passivation.

221

222 **A minimal CTRW model recapitulates the diffusion of all NPs**

223

224 As shown, the cytoplasmic mobility of particles of similar size (~25 nm) varied over several
225 orders of magnitude, with median instantaneous diffusivity coefficients $D_{60\text{ms}}$ ranging from
226 $0.005\mu\text{m}^2 \cdot \text{s}^{-1}$, for QDs without any additional surface coating (QDs-Itk-COOH), up to
227 $1\mu\text{m}^2 \cdot \text{s}^{-1}$ for Rho-NPs. Additionally, we observed both Brownian and anomalous diffusion.
228 We thus wondered if this large variability of cytoplasmic mobility could be recapitulated in a
229 simple, unified framework. First, we supposed the diffusion coefficient of a perfectly inert 25
230 nm object to be $10\mu\text{m}^2 \cdot \text{s}^{-1}$, a value corresponding to the fastest intracellular diffusion
231 coefficient reported in the literature for objects (dextran polymers²⁹) of that size. We next
232 hypothesized that non-specific interactions would affect the diffusive properties of NPs
233 through transient binding to immobile or slowly moving objects. Specifically, we considered
234 a continuous time random walk (CTRW) model with a waiting (immobilization) time
235 distribution, $P(t)$, between each step of the walk, of the form: $P(t) = \gamma \cdot t_0^\gamma / t^{1+\gamma}$ (defined for
236 $t > t_0$). The lower bound t_0 of the distribution is taken here to be the acquisition time and γ is a
237 positive parameter, encompassing the strength of non-specific interactions. The mean waiting
238 time $\langle t \rangle = \int_{t_0}^{\infty} tP(t)dt$ is equal to $\gamma t_0 / (\gamma - 1)$ for $\gamma > 1$ and diverges for $0 < \gamma \leq 1$. For
239 large γ , the mean immobilisation time is close to t_0 and it increases for decreasing γ values.

240

241 We simulated trajectories using our minimal CTRW model for different values of γ using
242 conditions similar to our experiments (see Methods). Remarkably, the simulated trajectories
243 recapitulated all the different behaviours observed. For very large γ (i.e. $\langle t \rangle \approx t_0$), simulated
244 trajectories showed free diffusion ($\alpha = 0.97 \pm 0.01$) and $D_{60\text{ms}} = 9.8 \pm 0.1\mu\text{m}^2 \cdot \text{s}^{-1}$, thus

245 very close to the value assumed for perfectly inert tracers (Fig. 4, $\gamma = \infty$). As γ decreases
246 toward 1, diffusion remained Brownian ($\alpha \sim 1$) but with reduced instantaneous diffusivity
247 coefficients $D_{60\text{ms}}$, due to the increasing mean immobilisation time (Fig. 4, $\gamma = 10$ to 1). This
248 regime recapitulated the diffusive properties of Rho-NPs. Interestingly, when γ was lower
249 than 1 (Fig. 4, $\gamma = 0.5$), the mean immobilisation time $\langle t \rangle$ diverged, the distribution in the α -
250 $D_{60\text{ms}}$ plane became elongated with a positive correlation as observed experimentally for QDs
251 (Fig. 1d). Finally, for very small values of γ (Fig. 4, $\gamma = 0.1$), because of the finite
252 observation time, trajectories could only probe a limited number of immobilisation times.
253 This resulted in a large variability in the mobility of individual objects and in a distribution in
254 the α - $D_{60\text{ms}}$ plane that recapitulated the feature observed for “naked” QDs (QDs-Itk-COOH).
255

256 Given the ability of our model to recapitulate the diffusivity of various NPs, we wondered if
257 we could find a perfectly inert NP in the same size range for which we should observe
258 Brownian diffusion with a diffusion coefficient close to $10\mu\text{m}^2 \cdot \text{s}^{-1}$. To this end, we probed
259 the mobility of ferritin NPs passivated with polyethylene glycols (PEGs), which have a size of
260 about 25 nm, thus similar to that of the other NPs analysed, and which were recently shown to
261 behave as highly inert probes³⁶. Remarkably, we observed a fast diffusion of ferritin NPs (Fig.
262 5, top-left panel) with a mean $D_{60\text{ms}} = 14.2 \pm 0.95\mu\text{m}^2 \cdot \text{s}^{-1}$ (median $D_{60\text{ms}} = 6.8\mu\text{m}^2 \cdot \text{s}^{-1}$),
263 about 10 times larger than for 25nm Rho-NPs and very close to the value expected for an
264 intracellular viscosity between 2 to 4 times that of water. The exponent α was 0.86 ± 0.01
265 lower than expected for purely Brownian particles, probably because of the broad distribution
266 of MSDs due to rapid (out-of-plane) motion of ferritin NPs and the consequent short exposure
267 time and fast frame rate required to track them.
268

269 Overall, our simple phenomenological model based on transient immobilisation is capable of
270 recapitulating all the diffusive properties observed in HeLa cells for the different NPs
271 analysed. The model also provides a ranking of NPs mobility according to the strength of
272 their non-specific interactions (Fig. 5, left panels). Remarkably, the ordered α - $D_{60\text{ms}}$ maps
273 show a very similar trend for a wide range of adherent mammalian cells, including primary
274 cells (Fig. 5). These results support the notion that the transport properties of NPs of similar
275 size are set by the physical nature of the cell interior and by the NPs surface properties rather
276 than by specific features of different cell types. Altogether, α - $D_{60\text{ms}}$ maps constitute a gauge
277 to assess the degree of non-specific interactions of NPs within the cytoplasm.
278

279 **Addressing the cytosolic diffusion of nano-sized objects**

280
281 Two major frameworks have long been competing to explain sub-diffusion in the cytosol, one
282 based on geometrical constraints³⁷ and one on biochemical interactions³⁸. For objects below
283 the “pore” size of the cytoplasm (defined as the interstitial size of the cytoplasm “solid”
284 matrix), our results unequivocally point to the predominant role of biochemical interactions.
285 The first and most compelling argument comes from the fact that if mobility would be
286 hindered by geometric obstructions all particles of the same physical size should be affected,
287 irrespective of their composition and surface properties. On the contrary, we found very
288 heterogeneous diffusive dynamics, including Brownian particles diffusing as fast as
289 $14\mu\text{m}^2 \cdot \text{s}^{-1}$. Thus, not only proteins³⁹ but also cytoplasmic objects with size of a few tens of
290 nanometres *can* diffuse freely in a fluid phase barely more viscous than water. The second
291 argument, based on the detailed analysis of QD trajectories, comes from the observed
292 ergodicity breaking which dismisses the geometrical argument in favour of the biochemical
293 hypothesis.

294

295 Yet, for NPs showing pronounced non-specific interactions, as for instance QDs-Itk-COOH,
296 one could wonder whether the reduced mobility might be caused by an increased effective
297 NPs size, due to a stable protein corona forming around them⁴⁰. However, as shown by Rho-
298 NPs data, the change in diffusivity between NPs of 15 and 50 nm is only a factor 2. Thus, a
299 putative corona effect cannot account for the spread over more than three orders of magnitude
300 observed for different types of NPs. Concerning the sub-diffusive behaviour of QDs, given
301 that time-averaged MSD curves have exponents smaller than one (mean $\alpha = 0.82$,
302 Supplementary Fig. 17), a subordinated diffusion process⁴¹, involving both ergodic
303 viscoelastic effects and non-ergodic immobilizations, could be invoked. Yet, if cytoplasm
304 would behave as a viscoelastic medium for probes of 25 nm in size, we should have observed
305 sub-diffusion for all the NPs employed. However, given that Rho-NPs showed Brownian
306 diffusion, we can exclude a role for cytoplasmic viscoelasticity at this particular scale.

307

308 In summary, we propose a unified framework to describe the diffusive dynamics of nano-
309 sized objects in the cytoplasm of eukaryotic cells (Fig. 6). First, as verified in HeLa cells and
310 in line with previous reports^{10,11,42}, diffusion is unconfined as long as the object size does not
311 exceed the pore size of the cytoplasm (between 50 and 75 nm). Above this size, diffusion is
312 restricted by the solid meshwork of the cell and movements of the probes, happening on
313 timescale of minutes, are mainly dictated by active stirring⁴³ and cytoskeleton dynamics^{44,45}.
314 Second, the intrinsic viscosity of the cytosolic fluid phase is low (2 to 4 time the viscosity of
315 water), confirming previous results^{29,30}. Third, diffusion can be slowed down by non-specific
316 interactions with intracellular components causing an increase of the apparent viscosity. If the
317 strength of interactions is weak, diffusion remains Brownian, whereas sub-diffusive behaviour
318 arises when the distribution of immobilisation times is broad enough so that the average
319 immobilisation time diverges. The nature of the components to which tracers bind is
320 presumably diverse; nevertheless, they have to be sufficiently immobile to considerably slow
321 down the diffusion of the interacting probes. These intracellular “binders” can be organelles,
322 vesicles, internal membranes, as well as macromolecular complexes bigger than the pore size,
323 thus undergoing constrained motion in the cytoplasm.

324

325 Importantly for further methodological developments, our tracking assay and the α - D_{60ms}
326 representation provide a quantitative benchmarking tool for the design of perfectly inert NPs.
327 The assay can be used to systematic screen the surface properties of NPs (such as the charge
328 or the nature of the surface passivation coating). In particular, our findings indicate that the
329 design of functionalization strategies for nanoparticle delivery⁴⁶ and manipulation⁴⁷ in the
330 cytoplasm, an important goal in nano-biosciences, should not be limited to testing endosomal
331 escape and cytosolic localization. It should also include the analysis of cytoplasmic mobility
332 of NPs, as it can dramatically vary and affect the ability of NPs to reach molecular targets
333 inside cells.

334

335

336 References

337

- 338 1. Bénichou, O., Chevalier, C., Klafter, J., Meyer, B. & Voituriez, R. Geometry-controlled
339 kinetics. *Nat. Chem.* **2**, 472–477 (2010).
- 340 2. Hellmann, M., Heermann, D. W. & Weiss, M. Enhancing phosphorylation cascades by
341 anomalous diffusion. *Europhys. Lett.* **97**, 58004 (2012).
- 342 3. Izeddin, I. *et al.* Single-molecule tracking in live cells reveals distinct target-search
343 strategies of transcription factors in the nucleus. *eLife* **3**, e02230 (2014).

- 344 4. Hou, L., Lanni, F. & Luby-Phelps, K. Tracer diffusion in F-actin and Ficoll mixtures.
345 Toward a model for cytoplasm. *Biophys. J.* **58**, 31–43 (1990).
- 346 5. Moeendarbary, E. *et al.* The cytoplasm of living cells behaves as a poroelastic material.
347 *Nat. Mater.* **12**, 253–261 (2013).
- 348 6. Luby-Phelps, K. Cytoarchitecture and physical properties of cytoplasm: volume,
349 viscosity, diffusion, intracellular surface area. *Int. Rev. Cytol.* **192**, 189–221 (2000).
- 350 7. Wojcieszyn, J. W., Schlegel, R. A., Wu, E.-S. & Jacobson, K. A. Diffusion of injected
351 macromolecules within the cytoplasm of living cells. *Proc. Natl Acad. Sci. USA* **78**,
352 4407–4410 (1981).
- 353 8. Tabaka, M., Kalwarczyk, T., Szymanski, J., Hou, S. & Holyst, R. The effect of
354 macromolecular crowding on mobility of biomolecules, association kinetics, and gene
355 expression in living cells. *Front. Phys.* **2**, 54 (2014).
- 356 9. Hofling, F. & Franosch, T. Anomalous transport in the crowded world of biological cells.
357 *Rep. Prog. Phys.* **76**, 046602 (2013).
- 358 10. Luby-Phelps, K., Taylor, D. L. & Lanni, F. Probing the structure of cytoplasm. *J. Cell*
359 *Biol.* **102**, 2015–2022 (1986).
- 360 11. Luby-Phelps, K., Castle, P. E., Taylor, D. L. & Lanni, F. Hindered diffusion of inert
361 tracer particles in the cytoplasm of mouse 3T3 cells. *Proc. Natl Acad. Sci. USA* **84**, 4910–
362 4913 (1987).
- 363 12. Jacobson, K. & Wojcieszyn, J. The translational mobility of substances within the
364 cytoplasmic matrix. *Proc. Natl Acad. Sci. USA* **81**, 6747–6751 (1984).
- 365 13. Yokoe, H. & Meyer, T. Spatial dynamics of GFP-tagged proteins investigated by local
366 fluorescence enhancement. *Nat. Biotechnol.* **14**, 1252–1256 (1996).
- 367 14. Klann, M. T., Lapin, A. & Reuss, M. Stochastic simulation of signal transduction: impact
368 of the cellular architecture on diffusion. *Biophys. J.* **96**, 5122–5129 (2009).
- 369 15. Banks, D. S. & Fradin, C. Anomalous diffusion of proteins due to molecular crowding.
370 *Biophys. J.* **89**, 2960–2971 (2005).
- 371 16. Regner, B. M. *et al.* Anomalous diffusion of single particles in cytoplasm. *Biophys. J.*
372 **104**, 1652–1660 (2013).
- 373 17. Nelson, S. R., Ali, M. Y., Trybus, K. M. & Warshaw, D. M. Random walk of processive,
374 quantum dot-labeled myosin Va molecules within the actin cortex of COS-7 cells.
375 *Biophys. J.* **97**, 509–518 (2009).
- 376 18. Dix, J. A. & Verkman, A. S. Crowding effects on diffusion in solutions and cells. *Annu.*
377 *Rev. Biophys.* **37**, 247–263 (2008).
- 378 19. Weiss, M., Elsner, M., Kartberg, F. & Nilsson, T. Anomalous subdiffusion is a measure
379 for cytoplasmic crowding in living cells. *Biophys. J.* **87**, 3518–3524 (2004).
- 380 20. Keren, K., Yam, P. T., Kinkhabwala, A., Mogilner, A. & Theriot, J. A. Intracellular fluid
381 flow in rapidly moving cells. *Nat. Cell Biol.* **11**, 1219–1224 (2009).
- 382 21. Barkai, E., Garini, Y. & Metzler, R. Strange kinetics of single molecules in living cells.
383 *Phys. Today* **65**, 29–35 (2012).
- 384 22. Fulton, A. B. How crowded is the cytoplasm? *Cell* **30**, 345–347 (1982).
- 385 23. Berry, H. & Chaté, H. Anomalous diffusion due to hindering by mobile obstacles
386 undergoing Brownian motion or Orstein-Uhlenbeck processes. *Phys. Rev. E* **89**, 022708
387 (2014).
- 388 24. Guigas, G., Kalla, C. & Weiss, M. The degree of macromolecular crowding in the
389 cytoplasm and nucleoplasm of mammalian cells is conserved. *FEBS Lett.* **581**, 5094–
390 5098 (2007).
- 391 25. Pinaud, F., Clarke, S., Sittner, A. & Dahan, M. Probing cellular events, one quantum dot
392 at a time. *Nat. Methods* **7**, 275–285 (2010).

- 393 26. Clarke, S. *et al.* Covalent monofunctionalization of peptide-coated quantum dots for
394 single-molecule assays. *Nano Lett.* **10**, 2147–2154 (2010).
- 395 27. Okada, C. Y. & Rechsteiner, M. Introduction of macromolecules into cultured
396 mammalian cells by osmotic lysis of pinocytotic vesicles. *Cell* **29**, 33–41 (1982).
- 397 28. Nandi, A., Heinrich, D. & Lindner, B. Distributions of diffusion measures from a local
398 mean-square displacement analysis. *Phys. Rev. E* **86**, 021926 (2012).
- 399 29. Luby-Phelps, K. *et al.* A novel fluorescence ratiometric method confirms the low solvent
400 viscosity of the cytoplasm. *Biophys. J.* **65**, 236–242 (1993).
- 401 30. Fushimi, K. & Verkman, A. S. Low viscosity in the aqueous domain of cell cytoplasm
402 measured by picosecond polarization microfluorimetry. *J. Cell Biol.* **112**, 719–725
403 (1991).
- 404 31. Récamier, V. *et al.* Single cell correlation fractal dimension of chromatin. A framework
405 to interpret 3D single molecule super-resolution. *Nucleus* **5**, 75–84 (2014).
- 406 32. Metzler, R., Jeon, J.-H., Cherstvy, A. G. & Barkai, E. Anomalous diffusion models and
407 their properties: non-stationarity, non-ergodicity, and ageing at the centenary of single
408 particle tracking. *Phys. Chem. Chem. Phys.* **16**, 24128–24164 (2014).
- 409 33. Meroz, Y. & Sokolov, I. M. A toolbox for determining subdiffusive mechanisms. *Phys.*
410 *Rep.* **573**, 1–29 (2015).
- 411 34. Weigel, A. V., Simon, B., Tamkun, M. M. & Krapf, D. Ergodic and nonergodic processes
412 coexist in the plasma membrane as observed by single-molecule tracking. *Proc. Natl*
413 *Acad. Sci. USA* **108**, 6438–6443 (2011).
- 414 35. Schulz, J. H. P., Barkai, E. & Metzler, R. Aging effects and population splitting in single-
415 particle trajectory averages. *Phys. Rev. Lett.* **110**, 020602 (2013).
- 416 36. Liße, D. *et al.* Monofunctional stealth nanoparticle for unbiased single molecule tracking
417 inside living cells. *Nano Lett.* **14**, 2189–2195 (2014).
- 418 37. Saxton, M. J. Anomalous diffusion due to obstacles: a Monte Carlo study. *Biophys. J.* **66**,
419 394–401 (1994).
- 420 38. Saxton, M. J. Anomalous diffusion due to binding: a Monte Carlo study. *Biophys. J.* **70**,
421 1250–1262 (1996).
- 422 39. Di Rienzo, C., Piazza, V., Gratton, E., Beltram, F. & Cardarelli, F. Probing short-range
423 protein Brownian motion in the cytoplasm of living cells. *Nat. Commun.* **5**, 5891 (2014).
- 424 40. Del Pino, P. *et al.* Protein corona formation around nanoparticles – from the past to the
425 future. *Mater. Horiz.* **1**, 301–313 (2014).
- 426 41. Tabei, S. M. A. *et al.* Intracellular transport of insulin granules is a subordinated random
427 walk. *Proc. Natl Acad. Sci. USA* **110**, 4911–4916 (2013).
- 428 42. Janson, L. W., Ragsdale, K. & Luby-Phelps, K. Mechanism and size cutoff for steric
429 exclusion from actin-rich cytoplasmic domains. *Biophys. J.* **71**, 1228–1234 (1996).
- 430 43. Guo, M. *et al.* Probing the stochastic, motor-driven properties of the cytoplasm using
431 force spectrum microscopy. *Cell* **158**, 822–832 (2014).
- 432 44. Tseng, Y., Kole, T. P. & Wirtz, D. Micromechanical mapping of live cells by multiple-
433 particle-tracking microrheology. *Biophys. J.* **83**, 3162–3176 (2002).
- 434 45. Hu, J. *et al.* Size- and speed-dependent mechanical behavior in living mammalian
435 cytoplasm. *Proc. Natl Acad. Sci. USA* **114**, 9529–9534 (2017).
- 436 46. Delehanty, J. B., Mattoussi, H. & Medintz, I. L. Delivering quantum dots into cells:
437 strategies, progress and remaining issues. *Anal. Bioanal. Chem.* **393**, 1091–1105 (2009).
- 438 47. Etoc, F. *et al.* Subcellular control of Rac-GTPase signalling by magnetogenetic
439 manipulation inside living cells. *Nat. Nanotechnol.* **8**, 193–198 (2013).

440

441

442 **Acknowledgment**

443

444 We acknowledge Maïté Coppey-Moisan (Institut Jacques Monod) for providing NIH 3T3 and
445 hMSC cells, Bruno Goud (Institut Curie) for RPE-1 cells, and Sébastien Letard and Patrice
446 Dubreuil (Centre de Recherche en Cancérologie de Marseille) for HDFa cells. E.B.
447 acknowledges the Ecole Doctorale Frontières du Vivant (FdV) – Programme Bettencourt for
448 financial support. MD and MC acknowledge financial support from French National Research
449 Agency (ANR) Paris-Science-Lettres Program (ANR-10-IDEX-0001-02 PSL), Labex
450 CelTisPhyBio (ANR-10-LBX-0038), the Human Frontier Science Program (grant no.
451 RGP0005/2007) and the France-BioImaging infrastructure supported by ANR Grant ANR-
452 10-INSB-04 (Investments for the Future). This project has received funding from the
453 European Union's Horizon 2020 Research and Innovation Programme under grant agreement
454 No 686841 (MAGNEURON).

455

456

457 **Author contributions**

458

459 F.E., M.D., and MC conceived the study. F.E. performed experiments and numerical
460 simulations. F.E. and D.N. did ferritin NPs experiments in HeLa cells. A.S. executed early
461 experiments. C.V. conducted the NPs release validation experiments. E.B. performed RPE-1
462 and hMSC experiments. D.N. collected HDFa data. D.L. and J.P. provided reagents. F.E.,
463 E.B., and M.C. analysed the data. All authors discussed the results and commented on the
464 manuscript. F.E., D.N., M.D., and M.C. wrote the manuscript.

465

466

467 **Competing financial interests**

468

469 The authors declare no competing financial interests.

470

471

472 **Methods**

473

474 **Cell culture.** HeLa and NIH 3T3 cells were cultured in $1.0 \text{ g} \cdot \text{l}^{-1}$ glucose, phenol-red free
475 DMEM (11054020, Gibco) supplemented with 10% (v/v) FBS (10270106, Gibco), $1 \times$
476 GlutaMAX™ (35050061, Gibco), and $100 \text{ U} \cdot \text{ml}^{-1}$ of penicillin/streptomycin (15140122,
477 Gibco). Primary normal, adult Human Dermal Fibroblast (HDFa, PCS-201-012™, ATCC®)
478 were cultured in $4.5 \text{ g} \cdot \text{l}^{-1}$ glucose, phenol-red free DMEM (31053028, Gibco) supplemented
479 with 10% (v/v) FCS (CVFSVF00-01, Eurobio), 1 mM Sodium Pyruvate (11360070, Gibco),
480 $100 \text{ U} \cdot \text{ml}^{-1}$ penicillin/streptomycin (15140122, Gibco), and $1 \times$ GlutaMAX™ (35050061,
481 Gibco). Retinal Pigmented Epithelial (RPE-1) cells were cultivated using DME/F-12 medium
482 (D8437, Sigma-Aldrich) supplemented with 10% (v/v) FBS (10270106, Gibco). Cells were
483 passed every 3 days when reaching 80-90% confluency. Human Mesenchymal Stem Cells
484 (hMSC, MSC-001F, StemCell) were cultivated with MesenCult™ proliferation kit (05411,
485 StemCell) in flask coated with type I collagen (C8919, Sigma-Aldrich). Cells were passed
486 every 10 days when reaching 70% confluency. All cells were maintained at 37°C in
487 humidified, CO₂-controlled (5%) incubators. HeLa cells were purchased from ATCC. NIH
488 3T3 and hMSC cells were provided by Maïté Coppey-Moisan (Institut Jacques Monod) and
489 originally obtained from ATCC and StemCell, respectively. RPE-1 cells were provided by
490 Bruno Goud (Institut Curie) and originally obtained from ATCC. HDFa cells were provided
491 by Sébastien Letard and Patrice Dubreuil (Centre de Recherche en Cancérologie de Marseille)
492 and originally obtained from ATCC.

493

494 **Nanoparticles.** The following quantum dots have been purchased from Thermo Fisher
495 Scientific: Qdot[®] Amino (PEG) 655 ITK[™] (reference Q21521MP, called “QDs” or “QDs-
496 PEG-NH₂” in the text); Qdot[®] 655 ITK[™] Carboxyl (reference Q21321MP, “QDs-Itk-COOH”
497 or “naked QDs” in the text); Qdot[®] 625 Streptavidin Conjugate (reference Q22063, “QDs-
498 streptavidin” in the text); Qdot[®] 605 ITK[™] Streptavidin Conjugate (reference Q10001MP,
499 “QDs-605” in Supplementary Information). “QDs-peptide” have been previously obtained in
500 the lab⁴⁸ and “QDs-COOH-PEG” were obtained by PEGylation of “QDs-Itk-COOH”. The
501 hydrodynamic radius of all quantum dots is 20 nm (Thermo Fisher Scientific, personal
502 communication). Red-emitting polystyrene/polymethacrylate NPs of different diameters
503 (“Rho-NPs” in the text) were made on our demand by micromod Partikeltechnologie GmbH
504 (Germany): 15 nm plain NH₂ (reference 30-01-151), 25 nm streptavidin (reference 30-19-
505 251), 50 nm streptavidin (reference 30-19-501), 75 nm streptavidin (reference 30-19-751).
506 Characterization of Rho-NPs size is reported in Supplementary Fig. 10. Ferritin-PEG-
507 Atto647N NPs (“ferritin NPs” in the text) have been previously obtained in the lab³⁶. The zeta
508 potential of NPs is reported in Supplementary Table 3.

509

510 **Nanoparticles internalization.** NPs internalization via pinocytosis in HeLa, NIH 3T3, and
511 HDFa cells was done on adherent cells, plated on glass coverslips the day before experiments,
512 following the manufacturer’s procedure (Influx[™] reagent, I14402 Thermo Fisher Scientific).
513 Cells were incubated 10 minutes at 37°C with hypertonic medium containing the desired NPs
514 at a concentration of ~15 nM. Then, coverslips were incubated vertically for two minutes in
515 hypotonic medium (serum free medium and deionized water in a 6:4 ratio) and washed
516 extensively with fresh medium. Pinocytosis in RPE-1 and hMSC cells was done using cells in
517 suspension according to the advices of the Influx[™] reagent provider. After being detached
518 from culture dishes, cells were pelleted at 300×g (RPE-1) or 450×g (hMSC) and then re-
519 suspended and incubated for 10 minutes with 20 µl of hypertonic solution with NP
520 concentrations on the order of 4 to 10 nM for QDs-Itk-COOH, QD-PEG-NH₂, and ferritin
521 NPs and of 90 nM for 25nm Rho-NPs. Next, 1 ml of hypotonic medium was added and, 1
522 minute after addition, cells were pelleted for 60 s. Total exposure to hypotonic medium
523 ranged between 150 s and 180 s. Cells were then re-suspended in fresh medium and washed at
524 least three times. Finally, cells were plated on glass coverslip previously incubated (30 min at
525 37°C) with 100 µg · ml⁻¹ type I collagen in PBS. In all cases, cells were let recover for at least
526 one hour in the incubator before imaging. For microinjection experiments (Supplementary
527 Fig. 7 and used for 75nm Rho-NPs internalization), glass pipettes with ~1 µm diameter
528 aperture were realized with a P-97 pipette puller (Sutter Instrument). Cell were injected using
529 a semi-automatic microinjection system (Injectman II, Epperndorf) with ~0.1 pl of NPs
530 solution (~15 nM in PBS), which represents about one tenth of the cell volume. Cell injection
531 was done within a small coverslip area marked by drawing a circle below the coverslip. After
532 injection, cells were placed in the incubator for one hour before imaging to ensure their
533 recover and osmolarity re-equilibration. For experiments involving drug treatments, after QDs
534 internalization, cells were incubated for one hour with the indicated concentration of drug
535 freshly diluted from concentrated DMSO stocks.

536

537 **Characterization of the NPs internalization.** The osmotic shock applied during pinocytosis
538 led to bursting of most of the ~2 µm-diameter pinocytotic vesicles (about 8 vesicles were
539 formed per cell) and to the delivery of 20 to 50 individual NPs per cell (Supplementary Fig.
540 1). After pinocytic treatment ~70% of cells were viable and we did not observe any additional
541 toxicity due to NPs (Supplementary Fig. 2). Remaining unburst vesicles (at most 3 per cell,
542 Supplementary Fig. 1) were systematically excluded when selecting regions of interest for

543 analysis (see Supplementary Video 1 and 2). Contrarily to NPs enclosed in unburst vesicles,
544 NPs released in the cytosol were able to diffuse in the whole cytoplasm, without entering into
545 the nucleus, and to efficiently target specific cellular components (Supplementary Fig. 3). In
546 the case of QDs, we observed blinking of the fluorescence signal, a typical signature of
547 individual emitters (Supplementary Fig. 4 and Supplementary Video 3) indicative of mono-
548 dispersed particles. When NPs of two distinct colours were co-internalized, no co-localization
549 or correlated dynamics were observed (Supplementary Fig. 5 and Supplementary Videos 4
550 and 5). We did not find significant differences in the behaviour of both 25nm Rho-NPs and
551 QDs when performing experiments in two different mammalian cell lines (HeLa and 3T3,
552 Supplementary Fig. 6) or when NPs were microinjected in cells, as an alternative
553 internalization method (Supplementary Fig. 7).

554
555 **Imaging.** Cells were imaged using thermalized (37°C), atmosphere-controlled (5% CO₂)
556 inverted microscopes, using high N.A. 100× oil-immersion objectives, and back-illuminated
557 EMCCDs for image acquisition. After NPs internalization, we selected 20 to 30 regions of
558 interest (~150×150 pixels) away from the cell nucleus and that did not contain unburst
559 vesicles, which were easily distinguished from single, diffusing NPs (see Supplementary
560 Video 1 and 2) thanks to their brightness and size (Supplementary Fig. 1). Each recording
561 lasted 1,000 frames and at least 12 cells were imaged for each experimental condition from at
562 least three different sample preparations. In HeLa, NIH 3T3, RPE-1, and hMSC cells
563 experiments, time-lapse images of diffusing QDs were recorded using a Xe lamp for UV epi-
564 fluorescence illumination, a bandpass filter (FF02-641/75-25, Semrock), and an exposure
565 time of 30 ms. Rho-NPs were imaged with an exposure time of 10 ms under wide field laser
566 excitation (561 nm) using a long pass dichroic filter with cut off at 573 nm (FF573-Di01-
567 25x36, Semrock) and an emission filter centred at 593 nm (FF01-593/46-25, Semrock).
568 Recordings of rapidly diffusing ferritin NPs were performed with 2 ms integration time using
569 a previously described setup⁴⁹ employing a 640 nm laser and a long pass emission filter
570 (BLP01-635R-25, Semrock). Two colours experiments (Supplementary Fig. 5 and
571 Supplementary Video 4 and 5) were executed using a dual-view beam splitter (Photometrics).
572 HDFa experiments have been conducted using HILO illumination⁵⁰ and a multi-band dichroic
573 for laser excitation (Di01-R405/488/561/635-25x36, Semrock). QDs have been excited with a
574 405 nm laser and imaged through a bandpass filter (FF01-676/37-25, Semrock) using 30 ms
575 exposure time. Rho-NPs have been observed under 561 nm laser excitation using a bandpass
576 filter (616/57, 489074, Zeiss) and 10 ms exposure time, while ferritin NPs have been imaged
577 with a 642 nm laser using a bandpass filter (FF01-676/37-25, Semrock) and 5 ms exposure
578 time.

579
580 **Trajectory analysis.** Two-dimensional projection (on the x - y plane) of cytoplasmic diffusion
581 of single NPs was recorded and analysed. Motion along the optical axis (z) was not
582 considered under the assumption that all directions are equivalent for diffusion within an
583 isotropic medium. Trajectories were reconstructed with the MATLAB (MathWorks) routine
584 MTT, which accounts for blinking in the trajectories⁵¹. Each dataset contained at least 140
585 trajectories lasting more than 40 time points. Individual trajectories were analysed with home
586 written MATLAB routines. Two-dimensional time-averaged mean squared displacements
587 were calculated using the formula $\langle r^2(\tau) \rangle_T = \langle [x(t + \tau) - x(t)]^2 + [y(t + \tau) - y(t)]^2 \rangle_T$,
588 where the average is done over all points of the trajectory separated by a time interval τ
589 (sliding average). To compute the time-averaged mean square displacement $\langle r_{60ms}^2 \rangle_T$ over 60
590 ms, we first performed a linear fit on the first points of the time-averaged MSD curves to
591 remove the intercept at time 0, which is on the order of 60 nm for QDs (representative dataset
592 for NPs intensities). As described by Michalet⁵², the accuracy in the determination of the

593 slope of the MSD, which equals $4D$ in the present case, is related to the number of points used
594 for the MSD fit. We compared the results obtained considering different numbers of points
595 for the fit (from 2 to 10) and found no significant variation in the α - D maps (Supplementary
596 Fig. 8a). Thus, we chose to fit the taMSDs curves up to 60 ms (2 to 6 points depending on the
597 data set), in order to make the comparison between all NPs relevant. The obtained
598 instantaneous diffusivities were called $D_{60\text{ms}}$. The ensemble average of taMSDs was
599 calculated following the same routine as in Ref. 34. The exponent α was obtained as single
600 fitting parameter from the log-log plot of taMSD using a general diffusion model $\langle r^2 \rangle_T \sim t^\alpha$.
601 We acknowledge that the offset of the MSD, due to the static and dynamic errors, should be
602 removed when fitting α either by performing a fit with one or two additional free parameters⁵³
603 or by removing a constant value. However, we found that the low statistics in the number of
604 frame for individual trajectories prevented us from performing a unconstrained multi-
605 parameter fit. Doing so, we obtained unrealistic values for α and the errors. Yet, for all
606 datasets with a mean diffusion coefficient greater than $0.1 \mu\text{m}^2 \cdot \text{s}^{-1}$, the MSDs at one time-lag
607 are at least one order magnitude larger than the pointing error and, thus, the bias in our
608 estimation can be neglected. α - $D_{60\text{ms}}$ maps were generated using the MATLAB function
609 *scattercloud*, which smoothens two-dimensional histograms. The contour lines (percentiles of
610 the probability density) were obtained using the MATLAB routine *ksbivardens*, which
611 performs a bivariate kernel density estimation, and the function *quantile*. For analysis of Rho-
612 NP subpopulations, we used a k -mean algorithm to cluster data points in the α - $D_{60\text{ms}}$ plane.
613 We used four clusters and grouped together the two clusters with largest $D_{60\text{ms}}$ values to
614 evaluate the fast population and the two with the smallest $D_{60\text{ms}}$ values for the slow population
615 (Supplementary Fig. 9).

616
617 **Trajectory simulations.** Brownian trajectories were simulated using MATLAB routines. The
618 time lag was fixed at $\Delta t = 10$ ms. Elementary Δx , Δy , and Δz steps were drawn from a normal
619 distribution with zero mean and variance equal to $\sqrt{2 \cdot D \cdot \Delta t}$, the diffusion coefficient D was
620 chosen to be $10 \mu\text{m}^2 \cdot \text{s}^{-1}$ (and $0.25 \mu\text{m}^2 \cdot \text{s}^{-1}$ for Supplementary Fig. 13c). Initially, one
621 particle was randomly distributed in a representative box of 10 by 10 μm and 1 μm height to
622 fit the experimental volume of detection, including the limited focal depth of the microscope.
623 The particle was then allowed to diffuse. Boundaries were considered to be reflective to take
624 into account the exchange of particles in the observation field at equilibrium. However, each
625 time a particle reached the boundaries, the trajectory was interrupted and a new one started to
626 mimic particle loss by the tracking software; otherwise, trajectories were interrupted when
627 they reached 500 time steps. Overall, the number of trajectories (4000) as well as the
628 trajectory length distribution matched the experimental data. Simulated trajectories were
629 subsequently analysed using the same routines used for the experimental ones. For CTRW
630 trajectories, the boundary conditions were relaxed in order to keep ideal, perfectly inert
631 particles, with a diffusion coefficient of $10 \mu\text{m}^2 \cdot \text{s}^{-1}$, in the computational volume for a time
632 sufficient to generate long enough trajectories. Specifically, the box linear dimensions were
633 expanded by a factor 10. Between subsequent steps, corresponding to elementary jumps
634 lasting 10 ms with $D = 10 \mu\text{m}^2 \cdot \text{s}^{-1}$, the particle was immobilized for a random waiting time T
635 sampled from the cumulative distribution $F(T > t) = (t_0/t)^\gamma$.

636
637 **Code availability.** Custom written MATLAB routines (for MATLAB version R2015a) for
638 trajectory analysis, numerical simulation, and density plot generation will be made available
639 to readers by the authors upon reasonable request.

640

641 **Data availability.** All the data supporting the findings of this study, within the article and its
642 supplementary information, will be made available to readers by the authors upon reasonable
643 request.

644

645 **References**

646

647 48. Clarke, S., Tamang, S., Reiss, P. & Dahan, M. A simple and general route for
648 monofunctionalization of fluorescent and magnetic nanoparticles using peptides.
649 *Nanotechnology* **22**, 175103 (2011).

650 49. Normanno, D. *et al.* Probing the target search of DNA-binding proteins in mammalian
651 cells using TetR as model searcher. *Nat. Commun.* **6**, 7357 (2015).

652 50. Tokunaga, M., Imamoto, N. & Sakata-Sogawa, K. Highly inclined thin illumination
653 enables clear single-molecule imaging in cells. *Nat. Methods* **5**, 159–161 (2008).

654 51. Sergé, A., Bertaux, N., Rigneault, H. & Marguet, D. Dynamic multiple-target tracing to
655 probe spatiotemporal cartography of cell membranes. *Nat. Methods* **5**, 687–694 (2008).

656 52. Michalet, X. Mean square displacement analysis of single-particle trajectories with
657 localization error: Brownian motion in an isotropic medium. *Phys. Rev. E* **82**, 041914
658 (2010).

659 53. Backlund, M. P., Joyner, R. & Moerner, W. E. Chromosomal locus tracking with proper
660 accounting of static and dynamic errors. *Phys. Rev. E* **91**, 062716 (2015).

661

662

663 **Figure Captions**

664

665 **Figure 1. NPs of similar size have different diffusive signatures.**

666 Two types of NPs (25nm Rho-NPs and QDs) were chosen as an example to show that tracers
667 of similar size (~25 nm) can have different cytoplasmic diffusion properties. **a**, Distribution of
668 the instantaneous diffusivity coefficient $D_{60\text{ms}}$ for 25nm Rho-NPs in HeLa cells ($N = 1314$
669 trajectories). **b**, Density plot in the α - $D_{60\text{ms}}$ plane for 25nm Rho-NPs. Colour code represents
670 the local density of trajectories normalized between 0 (blue) and 1 (red). Black dots
671 correspond to individual trajectories ($N = 309$ trajectories lasting more than 40 frames, out of
672 1314 recorded trajectories). Black lines (contours) indicate 25, 50, and 75 percentiles. White,
673 dashed lines are a guide to the eye. **c**, Distribution of $D_{60\text{ms}}$ for QDs in HeLa cells ($N = 1696$
674 trajectories). **d**, Density plot in the α - $D_{60\text{ms}}$ plane for QDs ($N = 525$ out of 1696 trajectories).
675 **e**, Cumulative distributions of $D_{60\text{ms}}$ for QDs in glycerol (black, $N = 5118$ trajectories), in
676 HeLa cells (green, $N = 1696$ trajectories), and for 25nm Rho-NPs in HeLa cells (blue, $N =$
677 1314 trajectories). **f**, Density plot in the α - $D_{60\text{ms}}$ plane for QDs in 80% (v/v) glycerol ($N = 273$
678 out of 5118 trajectories). $D_{60\text{ms}}$ is expressed in $\mu\text{m}^2 \cdot \text{s}^{-1}$.

679

680 **Figure 2. Cytoplasmic mobility is strongly reduced for NPs above 50 nm in size.**

681 Representation of Rho-NPs trajectories in the α - $D_{60\text{ms}}$ plane in HeLa cells for **a**, 15nm Rho-
682 NPs ($N = 186$), **b**, 25nm Rho-NPs ($N = 309$), **c**, 50nm Rho-NPs ($N = 837$), and **d**, 75nm Rho-
683 NPs ($N = 202$). $D_{60\text{ms}}$ is expressed in $\mu\text{m}^2 \cdot \text{s}^{-1}$.

684

685 **Figure 3. QDs show intrinsic sub-diffusive behaviour and ergodicity breaking.**

686 **a**, Ensemble average of time-averaged MSDs, $\langle\langle r^2 \rangle_T\rangle_E$, in log-log scale obtained considering
687 all individual time-averaged MSDs ($N = 1696$ trajectories). The sub-diffusive behaviour of
688 QDs is evidenced by the deviation of QDs MSD curve (red data points) from the blue straight
689 line corresponding to Brownian diffusion (slope = 1). Data points represent mean values and
690 error bars are standard error of the mean. **b**, $\langle\langle r^2 \rangle_{T \geq N\Delta t}\rangle_E$ computed by considering only

691 trajectories lasting more than 30 (blue crosses, $N = 690$ trajectories), 70 (green circles, $N =$
692 289 trajectories), or 150 (red triangles, $N = 100$ trajectories) frames. MSD curves of QDs
693 trajectories homogeneous in length are linear in log-log scale, with an identical slope ~ 0.82 .
694 **c-d**, Temporal (top) versus ensemble (bottom) distributions of $D_{60\text{ms}}$ for QDs in (c) HeLa cells
695 ($N = 650$ trajectories lasting more than 40 frames, out of 1696 trajectories) and (d) in 80%
696 (v/v) glycerol ($N = 1512$ trajectories lasting more than 10 frames, out of 5118 trajectories).
697 Temporal distribution in (c) proceeds from Fig. 1c, while the ensemble distribution was
698 obtained through the following procedure: one value of the ensemble-averaged MSDs was
699 built by averaging the 60 ms-square displacements for all NPs detected at a given time point
700 of the acquisition, and the distribution of ensemble-averaged MSDs was obtained by
701 performing this average for all time points of the acquisition. **e**, Cumulative distribution of
702 $\log(D_{60\text{ms}})$ for QDs with five different surface coatings in HeLa cells: QDs-Itk-COOH (black,
703 $N = 915$ trajectories), QDs-peptide (red, $N = 785$ trajectories), QDs-COOH-PEG (green, $N =$
704 6531 trajectories), QDs-streptavidin (blue, $N = 685$ trajectories), QDs-PEG-NH₂ (purple, $N =$
705 1696 trajectories). Note that QDs-PEG-NH₂ are referred as QDs in the text. $D_{60\text{ms}}$ is expressed
706 in $\mu\text{m}^2 \cdot \text{s}^{-1}$.

707

708 **Figure 4. A minimal CTRW model recapitulates all the different NPs diffusive**
709 **behaviours observed.**

710 Representation in the α - $D_{60\text{ms}}$ plane of simulated trajectories obtained using a simple CTRW
711 model with different values of γ : ∞ , 10, 2, 1, 0.5, and 0.1. For large values of γ , corresponding
712 to perfectly inert probes, diffusion is fast ($D_{60\text{ms}} \sim 10 \mu\text{m}^2 \cdot \text{s}^{-1}$) and Brownian. When γ is
713 equal to 1 (the critical value of the immobilisation time to be integrable), diffusion is slowed
714 down by one order of magnitude ($D_{60\text{ms}} \sim 1 \mu\text{m}^2 \cdot \text{s}^{-1}$) but still Brownian, as observed for Rho-
715 NPs. When γ is further decreased ($\gamma = 0.5$), the immobilisation time diverges, the diffusion
716 coefficient drops by one more order of magnitude and sub-diffusive behaviour, together with
717 the “coma” shape in the α - $D_{60\text{ms}}$ plane, emerges, as observed in the case of QDs-PEG-NH₂
718 ($D_{60\text{ms}} \sim 0.1 \mu\text{m}^2 \cdot \text{s}^{-1}$ and $\alpha \sim 0.8$). The case $\gamma = 0.1$ corresponds to strongly sub-diffusing
719 objects immobilised almost all the time, as “naked” QDs (QDs-Itk-COOH). In each density
720 map, $N = 4000$ simulated trajectories. $D_{60\text{ms}}$ is expressed in $\mu\text{m}^2 \cdot \text{s}^{-1}$.

721

722 **Figure 5. NPs diffusivity can be ranked by the strength of non-specific interactions.**

723 Representation in the α - $D_{60\text{ms}}$ plane of trajectories obtained from experiments with different
724 NPs of similar size (~ 25 nm) in HeLa cells, in adult Human Dermal Fibroblasts (HDFa), in
725 Retinal Pigmented Epithelial (RPE-1) cells, and in human Mesenchymal Stem Cells (hMSC).
726 Data are sorted as a function of the instantaneous diffusivity coefficient $D_{60\text{ms}}$. The minimal
727 CTRW model suggests that such an ordering correlates with the strength of NPs non-specific
728 interactions with immobile, or slowly moving, intracellular components. The number N of
729 trajectories included the α - $D_{60\text{ms}}$ maps is (from top to bottom): 687, 309, 525, 389 for HeLa;
730 831, 1622, 237, 113 for HDFa; 469, 747, 466, 142 for RPE-1; and 645, 266, 168, 296 for
731 hMSC. $D_{60\text{ms}}$ is expressed in $\mu\text{m}^2 \cdot \text{s}^{-1}$.

732

733 **Figure 6. General model of cytosolic mobility.**

734 Objects (red spheres) that have size larger than the cytoskeleton mesh size (between 50 and
735 70 nm) are trapped in a viscoelastic medium and experience restricted diffusion. On time
736 scales of seconds, such large objects are confined, whereas they will move at longer time
737 scales thanks to the remodelling of internal structures (cytoskeleton, endomembranes).
738 Objects with size smaller than the pore size diffuse in a liquid phase whose apparent viscosity
739 depends on the strength of the biochemical interactions. If objects are perfectly inert, they

740 diffuse freely without hindering due to obstacles. The apparent viscosity is then slightly
741 higher than that of water. When objects start to interact with immobile and slowly moving
742 intracellular components, diffusion is slowed down but remains Brownian if the
743 immobilisation time does not exceed the time scale over which diffusion is measured. If the
744 strength of interactions increases up to the point that the immobilisation time can be longer
745 than the observation time, the diffusion is further slowed down and become anomalous.

Non-specific interactions govern cytosolic diffusion of nano-sized objects in mammalian cells

Fred Etoc^{1,§}, Elie Balloul^{1,†}, Chiara Vicario^{1,†,§}, Davide Normanno^{1,2,*}, Domenik Liße³,
Assa Sittner⁴, Jacob Piehler³, Maxime Dahan^{1,*}, Mathieu Coppey^{1,*}

¹ Laboratoire Physico-Chimie, Institut Curie, CNRS UMR168, PSL Research University, Université Pierre et Marie Curie-Paris 6. 11 rue Pierre et Marie Curie, 75248 Paris - Cedex 05, France

² Centre de Recherche en Cancérologie de Marseille, CNRS UMR7258, Inserm U1068, Aix-Marseille Université UM105, Institut Paoli-Calmettes. 27 boulevard Leï Roure, 13273 Marseilles - Cedex 09, France

³ Division of Biophysics, Department of Biology, Osnabrück University. BarbarasträÙe 11, 49076 Osnabrück, Germany

⁴ Department of Infectious Diseases, Israel Institute for Biological Research. POB 19, 7410001 Ness Ziona, Israel

† Equally contributed to this work

§ current address:

Center for Studies in Physics and Biology, The Rockefeller University. 1230 York Avenue, New York, NY 10065, USA (F.E.). Centre for Genomic Regulation, The Barcelona Institute of Science and Technology. Carrer del Dr. Aiguader 88, 08003 Barcelona, Spain (C.V.)

* Correspondence should be addressed to D.N. (davide.normanno@inserm.fr), M.D. (maxime.dahan@curie.fr), and M.C. (mathieu.coppey@curie.fr)

Supplementary Video Legends

Supplementary Video 1

Representative video of 25nm Rho-NPs diffusing in a HeLa cell after pinocytic loading. Three unburst vesicles can be seen at the top of the images: two very, close together, on the left and one, very bright, in the middle. These unburst vesicles are much larger than individual NPs and are basically immobile. Images were acquired every 10 ms, the video is encoded at 30 frames per second (fps). Scale bar represents 10 μm .

Supplementary Video 2

Representative videos of 25nm Rho-NPs diffusing in HeLa cells after pinocytic loading. Top row: crops of the field of view showing unburst vesicles. NPs encapsulated within these intact vesicles move very fast and cannot be tracked individually. Bottom row: examples of typical regions of interest chosen for NPs single-particle tracking analysis and selected in a way such that unburst vesicles were systematically excluded. The marked difference in the behaviour of free versus encapsulated NPs ensures a reliable discrimination between the two cases. Images were acquired every 10 ms, the video is encoded at 30 fps. Scale bars represent 1 μm .

Supplementary Video 3

Representative video of QDs (QDs-PEG-NH₂) diffusing in a HeLa cell after pinocytic loading. QDs clearly show *on-off* fluctuations (blinking) of the fluorescence signal (use Supplementary Fig. 4 as reference to more easily spot blinking particles). The blinking behaviour is a typical signature of individual emitters and indicates that QDs are mono-dispersed, confirming their escape from pinocytic vesicles and dismissing potential aggregations. Images were acquired every 30 ms, the video is encoded at 15 fps. The counter indicates the frame number. Scale bar represents 2 μm .

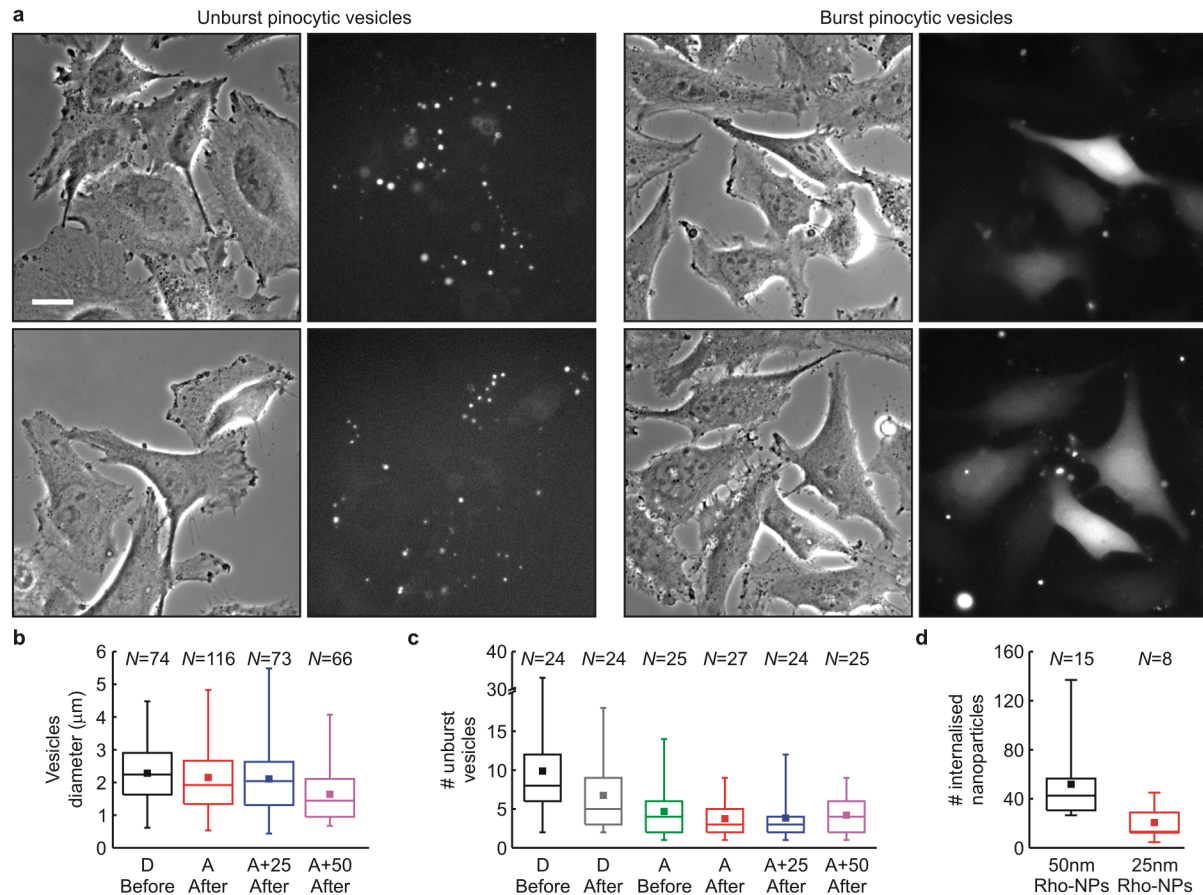
Supplementary Video 4

Representative video of the simultaneous diffusion of two different types of QDs, QDs-605 emitting at 605 nm (green) and QDs-PEG-NH₂ emitting at 655 nm (red), after concomitant pinocytic internalization. The images clearly illustrate that in the two HeLa cells visible in the video there is no co-localization of the two probes, on the contrary of what expected if NPs would have been still encapsulated inside unburst vesicles. Images were acquired every 30 ms, the video is encoded at 15 fps. Scale bar represents 5 μm .

Supplementary Video 5

The video shows the concurrent detection of the two types of QDs displayed in Supplementary Video 4: QDs-605 (red circles) and QDs-PEG-NH₂ (yellow circles). The images put well in evidence the absence of correlated dynamics in the mobility of the two probes, on the contrary of what expected if NPs would have been still encapsulated inside unburst vesicles. Images were acquired every 30 ms, the video is encoded at 10 fps. Scale bar represents 5 μm .

Supplementary Figure 1



Supplementary Figure 1 | Characterization of pinocytic internalization

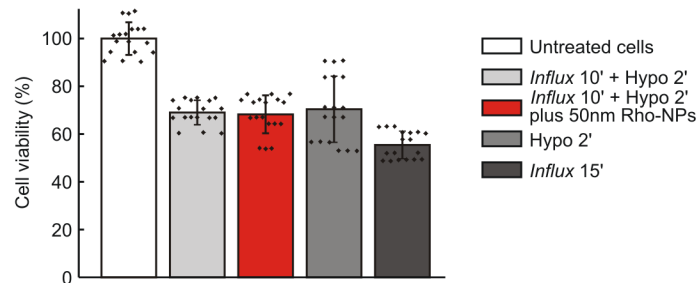
a) Formation and bursting of pinocytic vesicles. Left. Representative phase contrast and fluorescence images of HeLa cells containing unburst vesicles after pinocytic loading using FITC-Dextran (MW 150 kDa, concentration ~ 5 nM). Several pinocytic vesicles are formed in each cell: they appear as bright spots in the fluorescence images and are also visible in phase contrast. The choice to use high molecular weight Dextran was instrumental and dictated by the fact that it prevented bursting of the vesicles permitting, therefore, to quantify by fluorescence imaging the size and number of vesicles formed during pinocytosis (see Panels b and c). In fact, because of their extreme sensitivity to osmolarity, pinocytic vesicles burst even upon a gentle wash or dilution of the hypertonic medium, which prevents to reduce the extracellular fluorescence background and, thus, to image intact vesicles when filled with NPs. **Right.** Representative phase contrast and fluorescence images of HeLa cells after pinocytic loading of Atto488 (MW ~ 1 kDa, concentration ~ 70 μ M) used to quantify the number of vesicles remaining intact after osmotic shock (see Panel c). Of note, the presence in the field of view of unstained cells confirms that Atto488 was internalized via pinocytosis and not via passive diffusion. Each experiment has been repeated twice. Scale bar represents 20 μ m.

b) Quantification of pinocytic vesicles size. Box plots of pinocytic vesicles size quantified from fluorescence images after intensity thresholding. The size of intact vesicles was measured in the case of two different loading procedures: 10 min of *Influx* treatment in the presence of FITC-Dextran (black, “D Before”), and 10 min of *Influx* treatment in the presence of Atto488 (red, “A After”) plus 25 nm (blue, “A+25 After”) or 50 nm (magenta, “A+50 After”) Rho-NPs followed by 2 min of hypotonic medium incubation. In all cases, vesicles ranged between about 1 and 4 μm (with a mean size of $\sim 2 \mu\text{m}$), thus, well above the point-spread-function of our imaging systems ($\sim 300 \text{ nm}$), which ensures that they can be easily distinguished from diffraction-limited NPs. Boxes indicate 25 to 75% of the underlying distribution, central lines represent median values, solid squares denote mean values, vertical bars cover the interval from 1 to 99% of the distribution. N represents the number of vesicles analysed.

c) Quantification of unburst vesicles number. Box plots of the number of intact vesicles per cell in the case of two different loading procedures: 10 min of *Influx* treatment in the presence of FITC-Dextran (black, “D Before”, showing an average of 8 vesicles formed per cell) or of Atto488 (green, “A Before”), and 10 min of *Influx* treatment in the presence of FITC-Dextran (grey, “D After”), Atto488 (red, “A After”) plus 25 nm (blue, “A+25 After”) or 50 nm (magenta, “A+50 After”) Rho-NPs followed by 2 min of hypotonic medium incubation (showing on average of at most 3 unburst vesicles per cell). Boxes indicate 25 to 75% of the underlying distribution, central lines represent median values, solid squares denote mean values, vertical bars cover the interval from 1 to 99% of the distribution. N represents the number of cells analysed.

d) Quantification of the number of released NPs per cell. Box plots of the number of internalized nanoparticles into individual HeLa cells after 10 min of *Influx* treatment followed by 2 min of hypotonic medium incubation. We found 52 ± 32 NPs per cell (mean \pm SEM) in the case of 50nm Rho-NPs (black) and 21 ± 13 for 25nm Rho-NPs (red). Boxes indicate 25 to 75% of the underlying distribution, central lines represent median values, solid squares denote mean values, vertical bars cover the interval from 1 to 99% of the distribution. N represents the number of cells analysed.

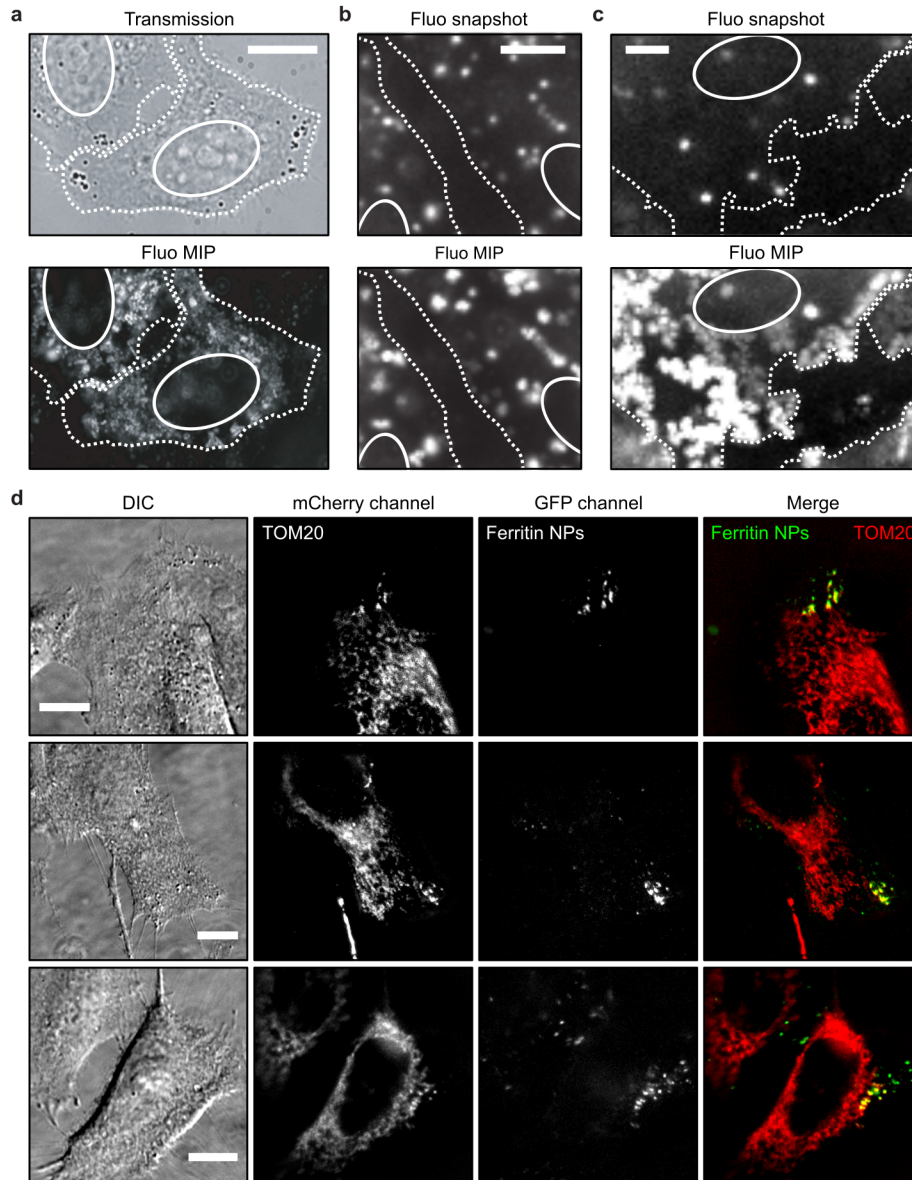
Supplementary Figure 2



Supplementary Figure 2 | Cells are largely viable after pinocytic internalization of 50nm Rho-NPs

Cell viability was measured using a MTT-based kit (M5655, Sigma-Aldrich) following the manufacturer procedure. HeLa cells were plated on 96-well plates and were either left untreated (white) or treated with the standard pinocytosis procedure: 10 min *Influx* reagent followed by 2 min of hypotonic medium incubation. In the latter case, about 70% of cells survived to the protocol irrespectively of the absence (light grey) or the presence (red) of 50nm Rho-NPs, indicating no additional cellular toxicity of NPs. Incubation with only hypotonic medium for 2 min (Hypo) resulted in similar levels of cell viability (grey) while longer incubation with the *Influx* reagent (e.g., 15 min) reduced cell viability to less than 60% (dark grey). Column values represent the average cell viability resulting from 18 independent wells (black diamonds) pulled together from three different experimental replicas. Error bars are standard deviations.

Supplementary Figure 3



Supplementary Figure 3 | NPs internalized via pinocytosis explore the whole cytoplasm and can target intracellular components

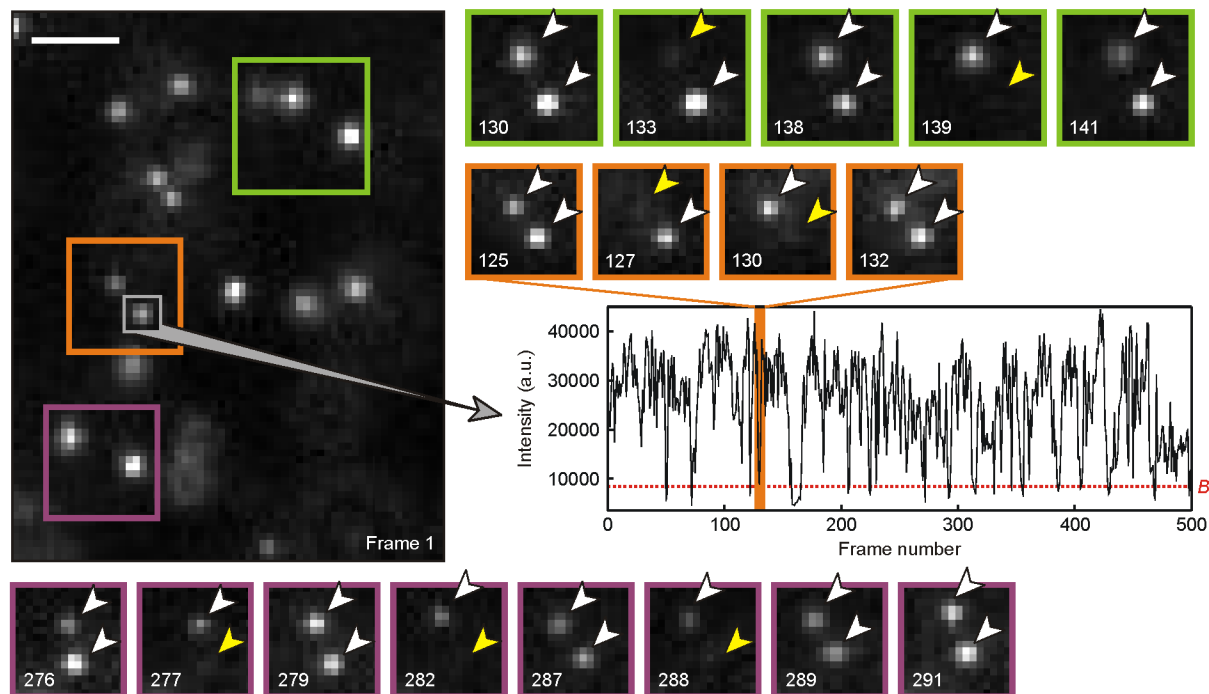
a) QDs behaviour after pinocytotic internalization. Top. Transmission image of two HeLa cells. **Bottom.** Maximum intensity projection (MIP) image of QDs fluorescence from a 2000 frame-long recording. QDs explore the whole cytoplasm of cells (white dotted contours), resulting in a diffuse fluorescence signal in the MIP image, but do not enter into the nuclei (white ovals), which remain dark. Internalization of QDs in living cells via pinocytosis has been achieved successfully more than 100 times. Scale bar represents 10 μm .

b) QDs intracellular exploration after passive endosomal internalization. **Top.** Snapshot of QDs fluorescence. **Bottom.** MIP of QDs fluorescence from a 500 frame-long recording. In this case, QDs remain trapped inside the endosomes (bright spots in both images) and do not move in the cytosol, resulting in no diffuse fluorescence signal in the MIP image. Passive endosomal internalization of QDs have been repeated twice. Scale bar represents 10 μm .

c) QDs intracellular exploration after pinocytic internalization. **Top.** Snapshot of QDs fluorescence. **Bottom.** MIP of QDs fluorescence from a 500 frame-long recording. Contrarily to when trapped inside endosomes (as in Panel b), after vesicles burst by osmotic shock QDs are released and explore the cytosol, resulting in a diffuse fluorescence signal in the MIP image. Pinocytic internalization of QDs have been successfully done more than 100 times. Scale bar represents 5 μm .

d) Targeting of ferritin NPs to mitochondria. Examples of HeLa cells expressing the chimeric construct GFPbinder-mCherry-TOM20 (localizing at the mitochondrial membrane) and loaded with ferritin-GFP-NPs using pinocytosis. **From left to right:** DIC images, mCherry channel, GFP channel, merge (yellow) of mCherry (red) and GFP (green) channels. Co-localization of fluorescence signals shows that ferritin-GFP-NPs could readily target mitochondria, indicating that NPs are dispersed in the cytosol and not encapsulated into pinocytic vesicles. Remarkably, targeting happened on small regions, presumably where vesicles burst, as the result of the very strong affinity (sub-nanomolar K_D) of the GFP-binder nanobody. The chimeric construct was realized fusing the GFP-binder nanobody and mCherry (used for visualization) to the cytosolic domain of TOM20. Ferritin-GFP-NPs were obtained fusing the heavy chain of ferritin to eGFP. Experiments have been repeated successfully three times. Scale bars represent 10 μm .

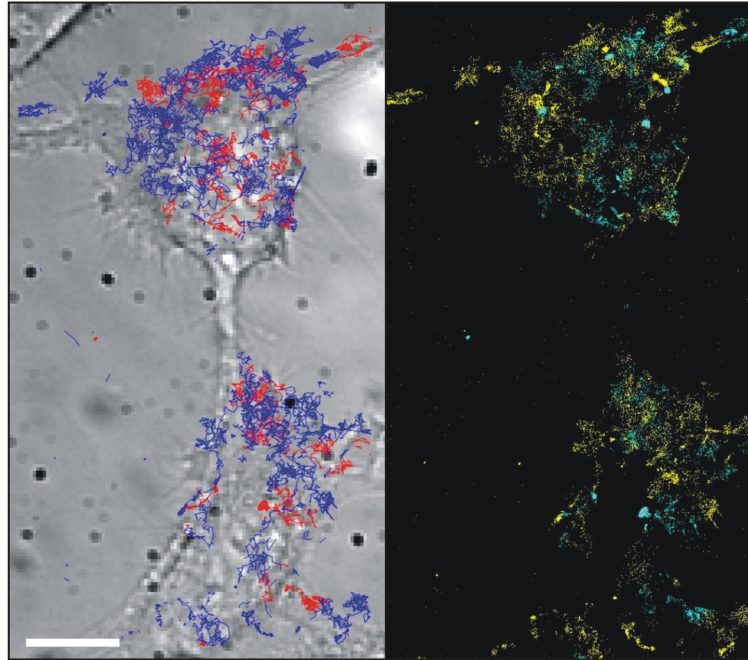
Supplementary Figure 4



Supplementary Figure 4 | QDs show blinking after pinocytic internalization

QDs internalized in HeLa cells via pinocytosis clearly showed *on-off* blinking of the fluorescent signal, a typical signature of individual emitters. This indicates that QDs are mono-dispersed, confirming their escape from pinocytic vesicles and dismissing potential aggregations (especially important in the case of QDs that are, possibly, the probe most prone to aggregate, given their very reactive core not fully screened by the outer functional coating, as evidenced by the results presented in the main text). The large image shows the first frame of Supplementary Video 3 and small crops show sub-sequent frames of the indicated coloured boxes, both for diffusing QDs (green and purple boxes) and for immobile QDs (orange box). In the latter case, the intensity of individual QDs could be easily followed over time integrating the signal of a small region around one NP (grey box). Fluctuations are clearly visible in the corresponding intensity time-course where the red dotted line indicates the background level B . White arrowheads point to emitting QDs (*on* state) while yellow arrowheads to dark QDs (*off* state). Numbers at the bottom left corner of the coloured boxes indicate the frame from which the image has been extrapolated. Blinking of individual QDs was successfully observed in three independent experiments. Scale bar represents 2 μm and applies to all images.

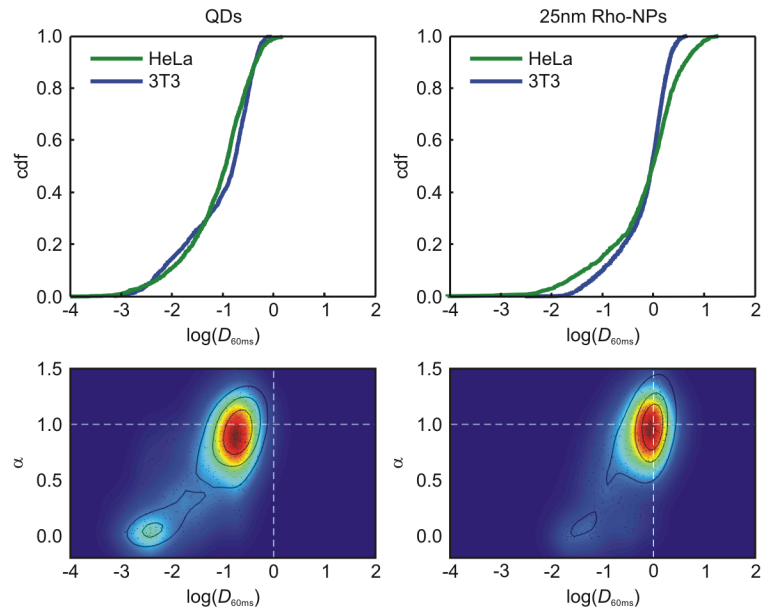
Supplementary Figure 5



Supplementary Figure 5 | QDs of different colours do not co-localize and diffuse independently after pinocytotic internalization

Left. Composite image showing two HeLa cells (grey scale) and the reconstructed trajectories of two different types of QDs simultaneously internalized via pinocytosis: QDs-605 emitting at 605 nm (red trajectories) and QDs-PEG-NH₂ emitting at 655 nm (blue trajectories). As visible, most trajectories span relatively large portions of the cells and do not show confinement within regions compatible with the size of pinocytotic vesicles (which have a diameter on the order of 2 μm). **Right.** Maximal projection image showing the detections of QDs-605 (cyan dots) and of QDs-PEG-NH₂ (yellow dots). No co-localization or correlated dynamics of the two types of QDs has been observed (see also Supplementary Video 4 and 5). Moreover, given the typical numbers of vesicles formed (~ 8) and of NPs internalized (between 20 and 50) per cell, the average number of NPs per vesicle is 4 and the probability that all the 8 vesicles formed, on average, in a given cell would be all filled with 4 NPs of the same colour is of the order of 10^{-8} , which -despite possible- is relatively improbable and further supports the effective release of NPs from pinocytotic vesicles. Dual colour experiments have been repeated twice and each time 10 cells have been imaged. Scale bar represents 5 μm .

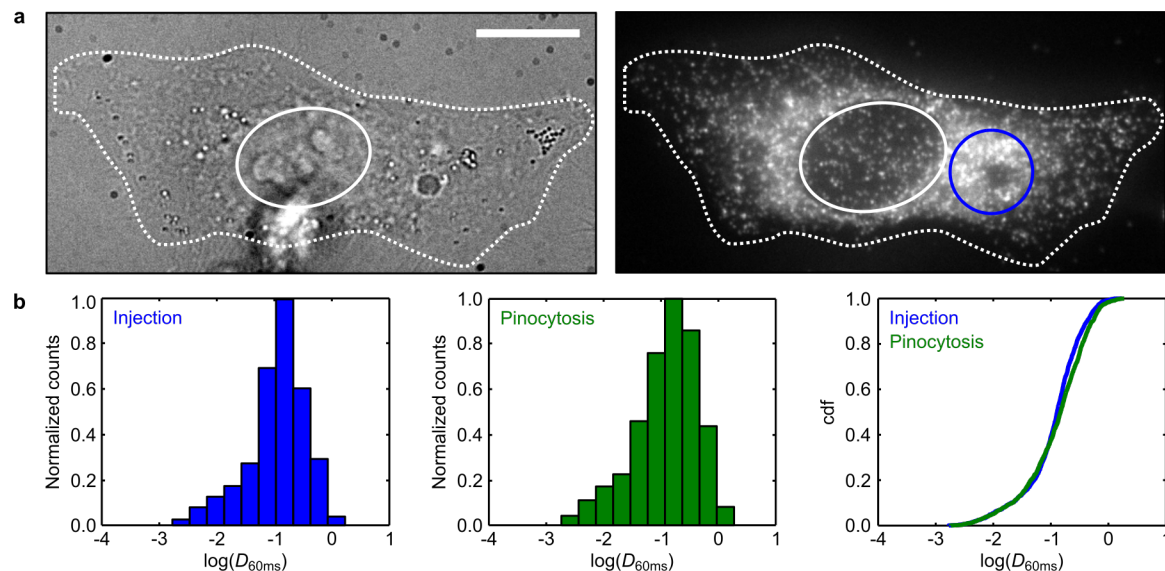
Supplementary Figure 6



Supplementary Figure 6 | QDs and 25nm Rho-NPs have similar diffusive properties in different mammalian cell lines

Top. Cumulative distribution function of the logarithm of the instantaneous diffusivity coefficients $D_{60\text{ms}}$ for QDs (left) and 25nm Rho-NPs (right) in human (cancerous) HeLa cells (green, $N = 1696$ trajectories for QDs and $N = 1314$ trajectories for Rho-NPs) and in murine (not cancerous) T3T fibroblasts (blue, $N = 1316$ trajectories for QDs and $N = 2768$ trajectories for Rho-NPs). No substantial quantitative differences emerged from experiments, suggesting uniformity of NPs behaviour in different mammalian cell lines. **Bottom.** Density plots in the α - $D_{60\text{ms}}$ plane for QDs (left, $N = 586$ trajectories lasting more than 40 frames, out of 1316 trajectories) and 25nm Rho-NPs (right, $N = 698$ trajectories lasting more than 40 frames, out of 2768 trajectories) in 3T3 fibroblasts. $D_{60\text{ms}}$ is expressed in $\mu\text{m}^2 \cdot \text{s}^{-1}$.

Supplementary Figure 7

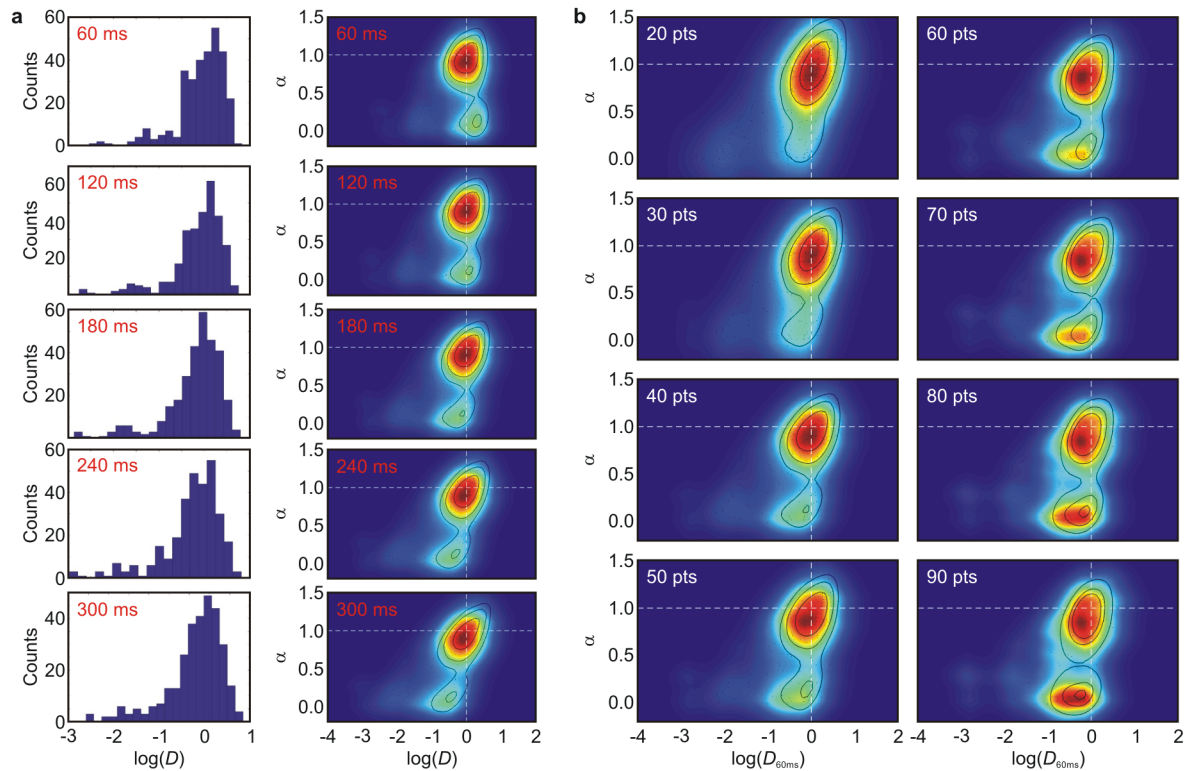


Supplementary Figure 7 | Microinjected NPs show identical diffusive properties than NPs internalized via pinocytosis

a) QDs microinjection. Left. Transmission image of a 3T3 cell (white dotted contour, white oval indicates the cell nucleus). **Right.** Corresponding fluorescence image of microinjected QDs. The microinjection locus is highlighted by the blue circle and contains a higher density of low mobility NPs. Microinjection experiments were repeated on more than 100 cells in four independent samples. Scale bar indicates 10 μm .

b) Comparison of NPs mobility for the two internalization methods. From left to right. Normalized distribution of the logarithm of $D_{60\text{ms}}$ for QDs microinjected in HeLa cells (blue). Normalized distribution of the logarithm of $D_{60\text{ms}}$ for QDs internalized in HeLa cells via pinocytosis (green). Cumulative distribution function of the logarithm of $D_{60\text{ms}}$ for QDs microinjected (blue) and internalized via pinocytotic loading (green) in HeLa cells. In both representations (histogram and cdf curve), $N = 1547$ trajectories of microinjected QDs and $N = 1696$ trajectories of QDs internalized via pinocytosis. $D_{60\text{ms}}$ is expressed in $\mu\text{m}^2 \cdot \text{s}^{-1}$.

Supplementary Figure 8



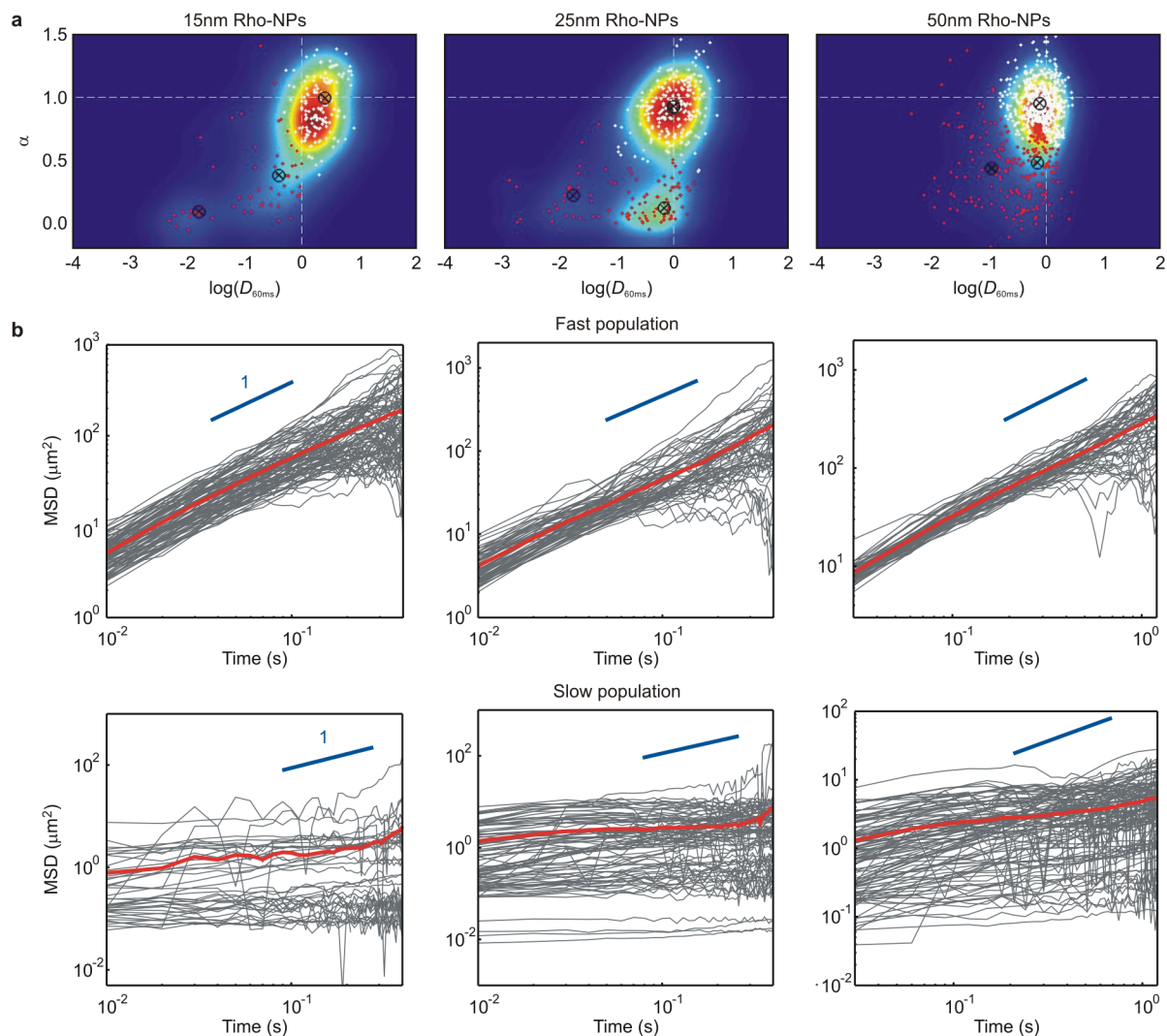
Supplementary Figure 8 | α - $D_{60\text{ms}}$ maps are robust with respect to the parameters used for their computation

a) Dependency on the time lag considered for the calculation of the instantaneous diffusivity coefficient D . Distributions of the logarithm of D (left) and α - D maps (right) computed considering increasing time lags (60, 120, 180, 240, and 300 ms) for the calculation of the instantaneous diffusivity coefficient D .

b) Dependency on the minimal trajectory length. α - $D_{60\text{ms}}$ maps computed considering an increasing minimal trajectory length (from 20 to 90 time points). Whereas the dependency on the time lag considered for the calculation of the instantaneous diffusivity coefficient D is marginal, the dependency of α - $D_{60\text{ms}}$ maps on the minimal trajectory length is more marked. In the results presented in the main text and in Supplementary Fig. 6 and 9, we used a minimal trajectory length of 40 time points to compute the α - $D_{60\text{ms}}$ maps. We considered that this choice represented a suitable trade-off between having trajectories long enough to limit data scattering in the maps but still short enough to avoid the strong bias towards severely sub-diffusive trajectories (which will have the tendency to remaining longer in the focal plane generating long trajectories), as highlighted by the results shown in Fig. 3a,b of the main text.

The dataset used for the analysis presented in both panels above is that relative to 25nm Rho-NPs internalized in HeLa cells via pinocytosis (same dataset used in Fig. 1b and Fig. 2b of the main text, $N = 309$ trajectories). D and $D_{60\text{ms}}$ are expressed in $\mu\text{m}^2 \cdot \text{s}^{-1}$.

Supplementary Figure 9

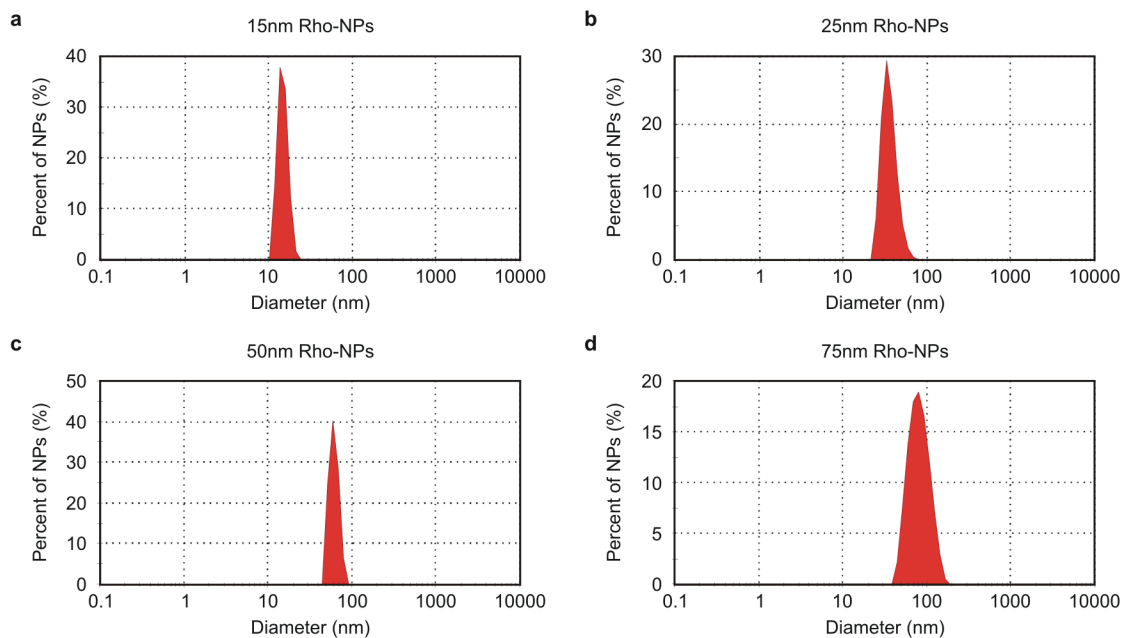


Supplementary Figure 9 | Identification and analysis of Rho-NPs subpopulations

a) Subpopulation identification via cluster analysis. To discriminate between fast and slow Rho-NPs subpopulations, we used the k -mean algorithm in MATLAB to cluster data points in the α - $D_{60\text{ms}}$ plane. Two clusters failed to satisfactorily separate the two subpopulations. Thus, we used four clusters and grouped together the two clusters with largest mean $D_{60\text{ms}}$ to select trajectories belonging to the fast population (white points in the maps), and the two clusters with the smallest mean $D_{60\text{ms}}$ to infer trajectories belonging to the slow population (red points in the maps). Cluster centroids are indicated by black crosses. Relative fractions and mean $D_{60\text{ms}}$ values of the two subpopulations are reported in Supplementary Table 1. 75nm Rho-NPs being mostly immobile, or very slowly diffusing, were not considered for the subpopulation analysis. The number of trajectories in the α - $D_{60\text{ms}}$ maps is: $N = 186$ for 15nm Rho-NPs, $N = 309$ for 25nm Rho-NPs, and $N = 837$ for 50nm Rho-NPs. $D_{60\text{ms}}$ is expressed in $\mu\text{m}^2 \cdot \text{s}^{-1}$.

b) MSD curves of fast and slow Rho-NPs subpopulations. Individual time-averaged MSDs (grey curves), in log-log scale, for the indicated Rho-NPs in HeLa cells after classification into fast (top row) and slow (bottom row) subpopulation with the cluster analysis. Blue lines have a slope of 1 (Brownian diffusion), red lines are ensemble averages. The fraction of trajectories in each of the two subpopulations is reported in Supplementary Table 1.

Supplementary Figure 10



Supplementary Figure 10 | Size distribution of Rho-NPs

Distribution of Rho-NPs diameter measured by dynamic light scattering (courtesy of micromod Partikeltechnologie GmbH).

a) 15nm (plain NH₂) Rho-NPs (product no. 30-01-151, lot no. 0030930-00) have a size of (15 ± 2) nm. $N = 8 \times 10^6$ particles.

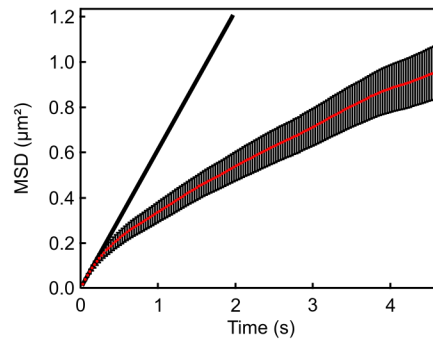
b) 25nm (streptavidin) Rho-NPs (product no. 30-19-251, lot no. 0451130-00) have a size of (35 ± 8) nm. $N = 12.1 \times 10^6$ particles.

c) 50nm (streptavidin) Rho-NPs (product no. 30-19-501, lot no. 0101230-1) have a size of (56 ± 9) nm. $N = 7.5 \times 10^6$ particles.

d) 75nm (streptavidin) Rho-NPs (product no. 30-19-751, lot no. 0211230-00) have a size of (77 ± 14) nm. $N = 27.7 \times 10^6$ particles.

Reported NPs size values are mean \pm SEM.

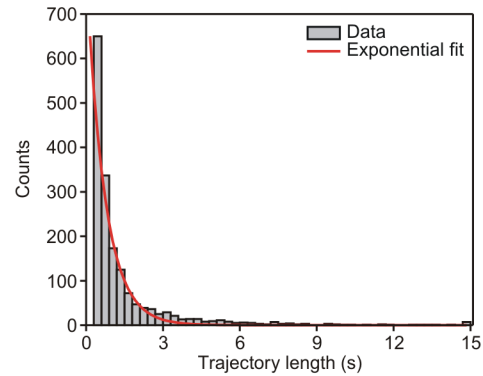
Supplementary Figure 11



Supplementary Figure 11 | The ensemble-averaged MSD of QDs is sub-linear

The graph shows (in linear scale) the ensemble average of all individual, temporally-averaged MSDs, $\langle\langle r^2 \rangle_T\rangle_E$, of QDs internalized in HeLa cells via pinocytosis ($N = 1696$ trajectories, same dataset than in Fig. 1c and Fig. 3a of the main text). The sub-linearity is clearly shown by the difference between the MSD curve obtained for QDs (red) and the straight line (black) corresponding to the MSD of a Brownian particle with a diffusion coefficient equal to the instantaneous diffusivity coefficient of QDs, $D_{60\text{ms}} = (0.15 \pm 0.01) \mu\text{m}^2 \cdot \text{s}^{-1}$. Error bars represent SEM.

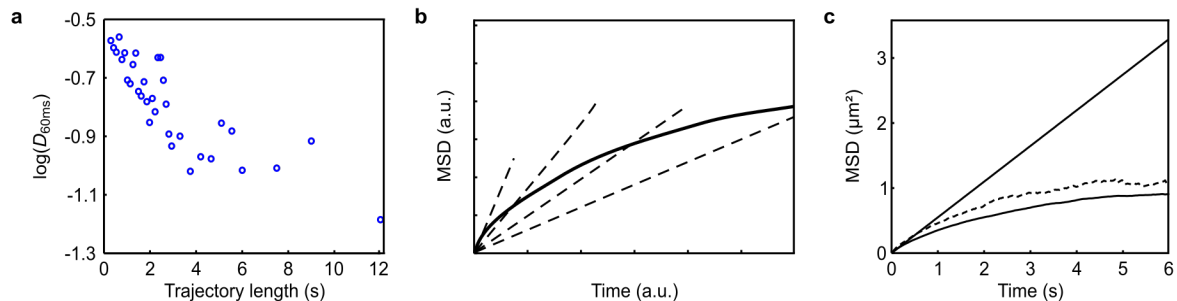
Supplementary Figure 12



Supplementary Figure 12 | Trajectory length follows an exponential distribution

The histogram (grey columns) shows the trajectory length distribution relative to QDs internalized in HeLa cells via pinocytosis. Red line represents the best fit to data using a mono-exponential decay function ($\tau = 0.7 \pm 0.1$ s). $N = 1696$ trajectories.

Supplementary Figure 13



Supplementary Figure 13 | Averaging of trajectories with different lengths results in artefactual sub-diffusivity

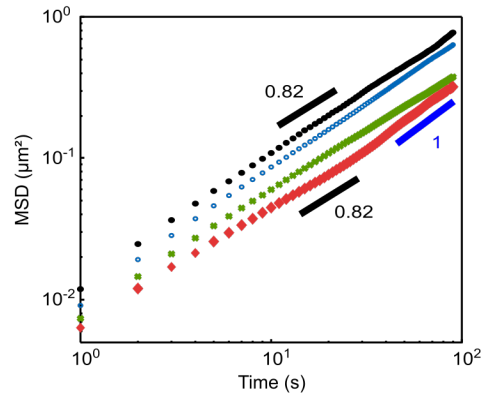
a) Dependence of $D_{60\text{ms}}$ on trajectory length. Scatter plot of the logarithm of the instantaneous diffusivity coefficient $D_{60\text{ms}}$ as a function of the trajectory length for QDs internalized via pinocytosis in HeLa cells ($N = 1696$ trajectories, binned into 34 intervals of different trajectory lengths). Data clearly indicate a negative correlation between $D_{60\text{ms}}$ and the trajectory length: the longer the trajectory the smaller the instantaneous diffusivity coefficient. As a consequence, length has a pronounced effect in trajectory analysis (as shown for 25nm Rho-NPs in Supplementary Fig. 8b) and, if not properly taken into account, it may profoundly affect the analysis of the ensemble behaviour of NPs (see Fig. 3a,b of the main text). Furthermore, at long time scales, the bias towards slow (and severely sub-diffusive) trajectories reflects into an accentuated, or even artefactual, sub-diffusive ensemble behaviour of NPs (see Panels b and c). $D_{60\text{ms}}$ is expressed in $\mu\text{m}^2 \cdot \text{s}^{-1}$.

b) Artefactual sub-diffusivity of averaged MSDs. The graph shows four fictive linear MSD curves (dashed lines). They represent theoretical MSDs of four Brownian particles with four different diffusion coefficients. As in experiments, rapidly diffusing particles leave quickly the observation volume, resulting in short trajectories and MSD curves extended over few time lags. Inversely, slowly diffusing particles have longer trajectories and MSD curves. Averaging of such not homogeneous, although linear, MSD curves gives rise to an artefactual sublinear ensemble MSD (solid line).

c) Ensemble averaging of Brownian trajectories -artificially generated from QDs data-shows sub-diffusion. For each recorded trajectory (of QDs in HeLa cells), we extracted two parameters: the trajectory length L and the instantaneous diffusivity coefficient $D_{60\text{ms}}$. From these two parameters, we build a set of linear MSD curves, each of them having duration L and slope determined by $D_{60\text{ms}}$. Remarkably, such an artificial set of perfectly Brownian MSDs resulted in a sub-diffusive ensemble-averaged MSD (dashed line), with approximately the same shape of the experimental one (solid line, same as red curve in Supplementary Fig. 11) and markedly deviating from Brownian diffusion (solid straight line).

Although rough, the calculations reported above (Panels b and c) highlight how sub-diffusive behaviour can emerge as an artefact inherent to the averaging over a set of purely Brownian trajectories with different length.

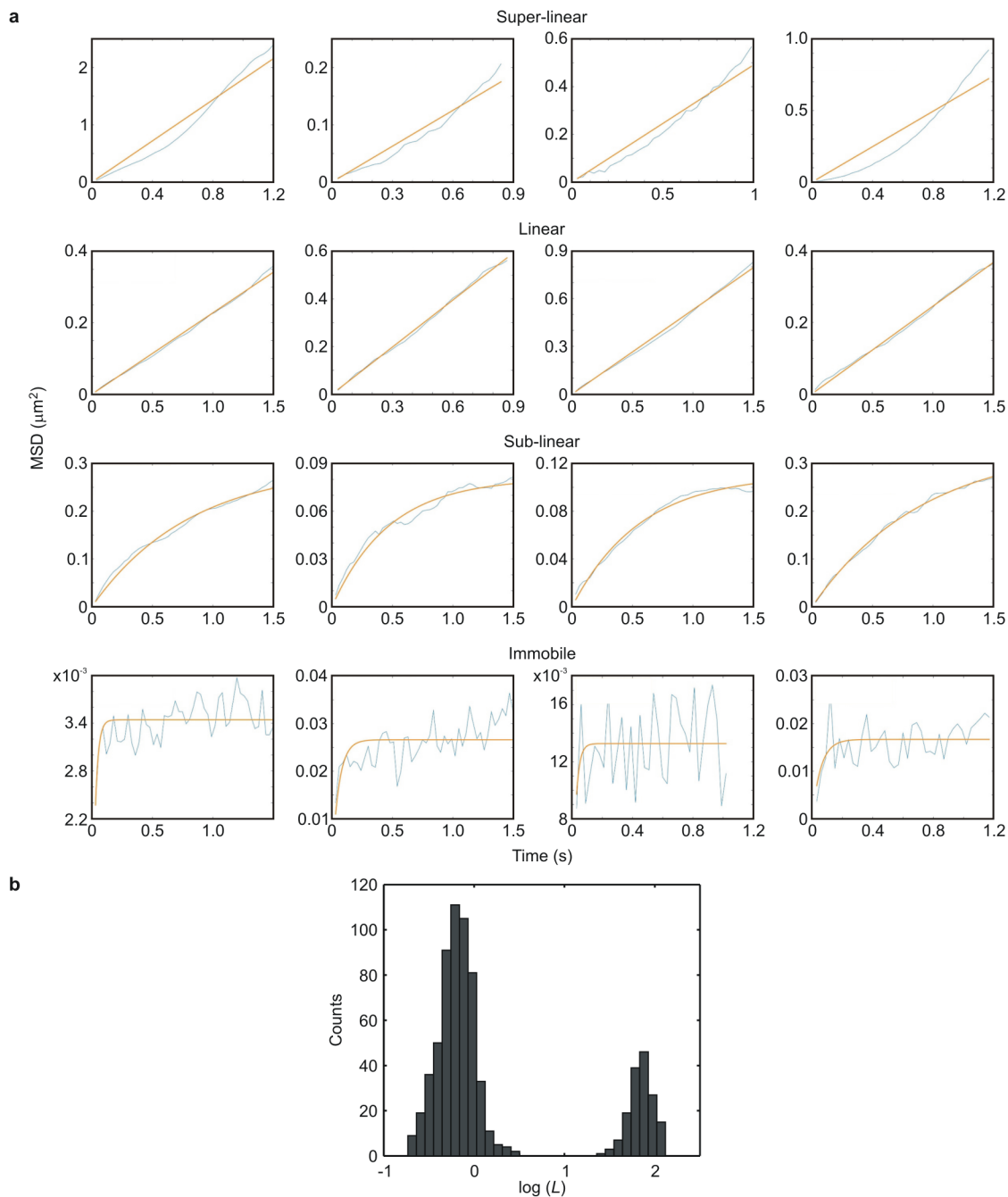
Supplementary Figure 14



Supplementary Figure 14 | Drug treatments have minor effects on QDs diffusive behaviour

The figure shows ensemble-averaged MSD curves of QDs in log-log scale, computed considering trajectories lasting more than 90 frames, obtained in HeLa cells after different drug treatments: basal conditions -untreated cells- (black), Nocodazole ($0.1 \mu\text{M}$) treated cells (blue), Latrunculin-A ($0.1 \mu\text{M}$) treated cells (green), Brefeldin-A ($5 \mu\text{M}$) treated cells (red). Despite slight variations in diffusivity (vertical spread of the curves), all MSDs are linear (in log-log scale) and, remarkably, they all have the same slope (0.82), pointing to an intrinsic anomalous behaviour of QDs, very mildly or not affected at all by the drug treatments used. In fact, only for Brefeldin-A treatment, and only at a long timescale, we could observe a deviation of the value of the MSD slope (from 0.82 to 1). QDs were internalised in HeLa cells via pinocytosis. Basal conditions: $N = 216$ trajectories lasting more than 90 frames, out of 1696 trajectories. Nocodazole treated cells: $N = 486$ trajectories out of 2189 trajectories. Latrunculin-A treated cells: $N = 312$ trajectories out of 1126 trajectories. Brefeldin-A treated cells: $N = 220$ trajectories out of 1101 trajectories.

Supplementary Figure 15



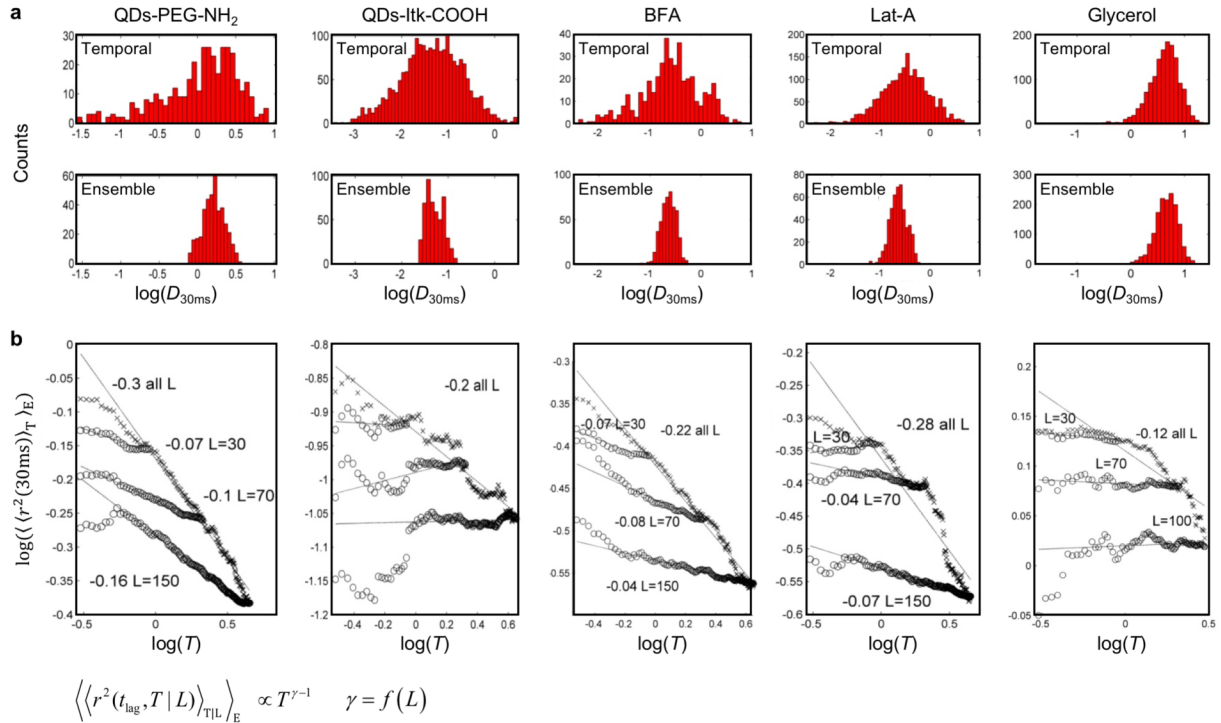
Supplementary Figure 15 | QDs mobility shows no strong evidence of confined diffusion

a) Confined diffusion fits of experimental MSD curves. Examples of time-averaged MSD curves, lasting more than 30 frames, obtained from QDs internalised in (untreated) HeLa cells via pinocytosis. MSD curves (cyan lines) have been fitted with a confined diffusion model (orange lines) using the formula: $\text{MSD}(t) = L^2 \cdot (1 - \exp(-12Dt/L^2))$, where L represents

the size of the confinement box and D the diffusion coefficient. Despite MSD curves are expected to be sub-linear in the case of confined diffusion, we found also linear –and even super-linear– MSDs. Overall, four different MSD categories emerged: super-linear, linear, sub-linear, and immobile (examples of each are shown in the four rows from top to bottom, respectively).

b) Box size distribution from confined diffusion fits in basal conditions. When we globally analysed the behaviour of QDs in HeLa cells, we obtained a bimodal distribution of the logarithm of the box size L (expressed in μm , $N = 685$ trajectories), which spanned more than three orders of magnitude. The highest values of L correspond to trajectories with linear or super-linear MSDs (as in the first two rows in Panel a) that, when fitted with a confined diffusion model (even if the residuals of the fit are small), are basically fitted by straight lines, resulting in unrealistic box sizes and no physical significance of the parameter L (i.e., L larger than the cell). Conversely, the second population with smaller values of L (77% of all trajectories) corresponds to trajectories (as in the third row in Panel a) fitted with a physically plausible box size, with a mean L value of 630 nm. Nevertheless, numerical simulations showed that a similar degree of confinement (box size) is found even for unrestricted, Brownian trajectories. In fact, due to the intrinsic variability of MSD curves, even a large fraction (60%) of simulated trajectories, of particles diffusing in free space, could be fitted with a confined diffusion model, resulting into a mean box size of 850 nm (see Supplementary Table 2 and Methods for details of simulations). This value does not differ significantly from the one found experimentally and, in our view, indicates that the (putative) box size found (for QDs) is mostly a consequence of the limited temporal window of observation of QDs dynamics. Furthermore, in no case (except for completely immobile QDs, as in the last row in Panel a) we could observe a clear plateau in the MSD of individual particles, the most unambiguous signature of confined diffusion. Finally, the different drug treatments tested did not provoke substantial changes in the estimates of the mean box size values nor in the percentage of confined trajectories while, contrarily to plausible expectations, they led to reduced box sizes and to increased percentages of confined trajectories (see Supplementary Table 2). We conclude that, overall, there is no strong evidence of confined diffusion for QDs.

Supplementary Figure 16



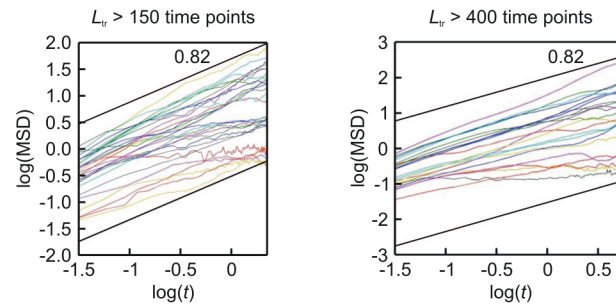
Supplementary Figure 16 | QDs trajectories show ergodicity breaking and aging

a) Ergodicity breaking. Temporal (top) versus ensemble (bottom) average distributions of the instantaneous diffusivity coefficients (calculated at 30 ms) for different probes (QDs-PEG-NH₂ and QDs-Itk-COOH) in basal conditions (untreated cells), and for QDs-PEG-NH₂ in cells treated with Brefeldin-A (BFA) or Latrunculin-A (Lat-A) or dispersed in glycerol (80% v/v in water). Ergodicity breaking is shown by the different broadness of the temporal and ensemble distributions observed in all cases but for glycerol. Experiments, except for glycerol were performed in HeLa cells and QDs internalized via pinocytosis. $D_{30\text{ms}}$ is expressed in $\mu\text{m}^2 \cdot \text{s}^{-1}$.

b) Aging. Ensemble average of time-averaged mean square displacements (calculated using the formula reported at the bottom and expressed in μm^2) for a lag time of 30 ms as a function of the truncation time T applied to the trajectories, for the above-mentioned probes and conditions. For QD-PEG-NH₂ in basal conditions, as well as after Latrunculin-A and Brefeldin-A treatments, we observed aging in trajectories, namely a power law dependency on the truncation time T . As indicated in the graphs, the exponent of the power law depends on the length L of the trajectories considered in the analysis. For “naked” QDs (QD-Itk-COOH), we did not observe aging, probably because of the extremely long binding times and the consequent low number of moving particles. Remarkably, as expected, QDs diffusing in glycerol did not show any sign of aging, on top of no sign of ergodicity breaking.

In both panels, the number N of trajectories included in the analysis is equal to 1696 for QDs-PEG-NH₂ in untreated cells, 915 for QDs-Itk-COOH in untreated cells, 1101 for QDs-PEG-NH₂ in Brefeldin-A treated cells, 1126 for QDs-PEG-NH₂ in Latrunculin-A treated cells, and 5118 for QDs-PEG-NH₂ in 80% (v/v) glycerol.

Supplementary Figure 17



Supplementary Figure 17 | Time-averaged MSD curves of QDs show sub-diffusive behaviour

The figure shows several different examples of individual time-averaged MSD curves, in log-log scale, for QDs trajectory with length (L_{tr}) lasting more 150 (left) and 400 (right) time points. Straight black lines represent the expected MSD for anomalous diffusion with an exponent α equal to 0.82. QDs (QDs-PEG-NH₂) were internalised in (untreated) HeLa cells via pinocytosis. Experiments have been repeated three times with similar results. MSD is expressed in μm^2 and t in seconds.

Supplementary Table 1

Rho-NPs diameter	Slow population			Fast population			$\eta_{\text{cyto}}/\eta_{\text{H}_2\text{O}}$
	Fraction	$D_{60\text{ms}}$ ($\mu\text{m}^2 \cdot \text{s}^{-1}$)	SEM ($\mu\text{m}^2 \cdot \text{s}^{-1}$)	Fraction	$D_{60\text{ms}}$ ($\mu\text{m}^2 \cdot \text{s}^{-1}$)	SEM ($\mu\text{m}^2 \cdot \text{s}^{-1}$)	
15 nm	0.30	0.33	0.04	0.70	2.50	0.14	13.6
25 nm	0.33	0.51	0.05	0.67	1.34	0.07	15.2
50 nm	0.29	0.54	0.03	0.71	0.94	0.02	10.9

Supplementary Table 1 | Mobility of 15nm, 25nm, and 50nm Rho-NPs

The Table reports the mobility parameters of the fast and slow population of Rho-NPs in HeLa cells obtained using the k -mean algorithm for subpopulation identification and separation (see Supplementary Fig. 9a and Methods for details).

Fraction indicates the subpopulation abundance, $D_{60\text{ms}}$ the mean diffusivity value and SEM the associated standard error of the mean.

η_{cyto} was calculated using the Stokes-Einstein equation: $D_{60\text{ms}} = k_{\text{B}}T / 6\pi\eta_{\text{cyto}}R$, where k_{B} is the Boltzmann constant, R the radius of the NPs, and considering the $D_{60\text{ms}}$ value relative to the fast population of NPs. In the calculation, the dynamic viscosity of water ($\eta_{\text{H}_2\text{O}}$) at 37°C has been assumed to be equal to $6.9 \times 10^{-4} \text{ N} \cdot \text{s} \cdot \text{m}^{-2}$.

The total number of trajectories considered in the analysis is $N = 186$ for 15nm Rho-NPs, $N = 309$ for 25nm Rho-NPs, and $N = 837$ for 50nm Rho-NPs.

Supplementary Table 2

	Basal conditions	Lat-A (100 nM)	Nocodazole (100 nM)	BFA (5 μM)	Simulated Brownian
Percentage of confined trajectories	77%	83%	75%	86%	60%
Mean box size	630 nm	500 nm	600 nm	478 nm	830 nm

Supplementary Table 2 | Effects of drug treatments on QDs confinement

The percentage of confined trajectories has been estimated from the relative amplitude of the two peaks in the bimodal distribution of the confinement box size (see Supplementary Fig. 15b). Mean box size represents the mean value of the peak with the smaller (and physically plausible) box size dimension (left peak in Supplementary Fig. 15b).

The results reported in the Table refer to QDs (QDs-PEG-NH₂) internalized in HeLa cells via pinocytosis in basal condition ($N = 1696$ trajectories) and after different drug treatments ($N = 1126$ trajectories for Lat-A; $N = 2189$ trajectories for Nocodazole; and $N = 1101$ trajectories for BFA), as well as for simulated Brownian trajectories ($N = 4000$ simulated trajectories). Lat-A stands for Latrunculin-A and BFA for Brefeldin-A.

As briefly mentioned in the caption of Supplementary Fig. 15b, if confinement would be effectively present and related to compartmentalization of the cytoplasm, treatments with drugs that affect the cytoplasm organization should induce a significant decrease of the fraction of confined QDs and/or an increase in the mean box size. Nevertheless, any change at all was found for cells treated with Nocodazole, a microtubule-depolymerizing drug. Treatment with Latrunculin-A or Brefeldin-A, which respectively disrupts the actin cytoskeleton and the Golgi apparatus, inversely to expectations, caused a slight decrease of the box size and a mild increase of the fraction of confined trajectories. Moreover, analysis of simulated trajectories showed that a large fraction (60%) of time-averaged MSDs of freely diffusing trajectories, with similar characteristics as those observed for QDs data (see Methods for details), could be as well fitted with a confined diffusion model, as a consequence of the intrinsic variability of Brownian motion and MSD curves, resulting in a mean box size of 850 nm.

Altogether, this suggests that the putative confinement found for QDs principally reflects the limited extent of the temporal window of observation of their dynamics and not real confined diffusion.

Supplementary Table 3

NPs	Zeta potential (mV)	Immobile fraction (%)	D_{60ms} ($\mu\text{m}^2 \cdot \text{s}^{-1}$)	
QDs-PEG-NH ₂	-6.5	36 ± 15	0.15	
QDs-streptavidin	-15	24 ± 6	0.16	
QDs-COOH-PEG	-10.5	13 ± 4	0.09	
QDs-peptide	-	46 ± 22	0.04	
QDs-Itk-COOH	-41.7	49 ± 19	0.025	
25nm Rho-NPs	-14.5	5 ± 3	D_{slow} 0.5	D_{fast} 1.34

Supplementary Table 3 | Properties and diffusivity of NPs of about 25nm-size

The diffusivity parameters (immobile fraction and D_{60ms} values) reported in the Table refer to NPs internalized in (untreated) HeLa cells via pinocytosis.

NPs are assumed to be immobile if their MSD curve is smaller than the pointing accuracy of our imaging systems (~60 nm). Errors on the immobile fraction are SEM.

The number of trajectories used for the calculation of the diffusivity parameters are: $N = 1696$ for QDs-PEG-NH₂, $N = 685$ for QDs-streptavidin, $N = 6531$ for QDs-COOH-PEG, $N = 785$ for QDs-peptide, $N = 915$ for QDs-Itk-COOH, and $N = 1314$ for 25nm Rho-NPs.